ELSEVIER

Earth and Planetary Science Letters 199 (2002) 287–310

EPSL

www.elsevier.com/locate/epsl

U–Pb isotopic behaviour of zircon during upper-amphibolite facies fluid infiltration in the Napier Complex, east Antarctica

Christopher J. Carson [a,*], Jay J. Ague [a], Marty Grove [b], Christopher D. Coath [b], T. Mark Harrison [b,1]

[a] *Department of Geology and Geophysics, Yale University, P.O. Box 208109, New Haven, CT 06520-8109, USA*
[b] *Department of Earth and Space Science, University of California, Los Angeles, CA 90095-1567, USA*

Received 8 August 2001; received in revised form 22 February 2002; accepted 28 February 2002

Abstract

Understanding the factors that contribute to U–Pb discordance in zircon is essential for interpreting isotopic data and for assessing the validity of concordia intercept ages. Modification caused by interaction with metamorphic fluids is often cited as a primary means by which significant or even complete isotopic resetting of U–Pb systematics in zircon might be achieved under subsolidus conditions. We present a field example from the Napier Complex, east Antarctica, in which a Palaeoproterozoic (2450–70 Ma) zircon population interacted locally with an Early Palaeozoic (498 ± 1.7 Ma) aqueous fluid at upper-amphibolite facies conditions. Conventional ion microprobe analysis of sectioned and polished grain surfaces indicates that fluid interaction resulted in minor disturbance of U and Pb in zircons (both normal and reverse discordance) with limited displacement along a chord with a lower intercept that coincides with the timing of fluid infiltration. In contrast, ion probe 'drilling' or depth profiling into unpolished natural zircon crystal surfaces revealed extensive disturbance of U–Pb systematics, to depths of ~ 0.2 μm, with near-surface ages consistent with the timing of fluid influx at ~ 498 Ma. Although zircon underwent some radiogenic Pb redistribution during fluid interaction, infiltrating fluids resulted in minimal *grain-scale* isotopic modification of zircon. Based on ion probe depth profiling results, we propose that limited normal discordance observed in the conventional ion microprobe zircon analyses, in this case, is controlled by an analytical mixture of reset and/or recrystallised zircon along penetrative micro-fracture networks with that of adjacent unaffected zircon. We also suggest that the observed reverse discordance is genuine, resulting from localised intra-grain net accumulations of radiogenic Pb. We conclude that the isotopic response of zircon, in this case, is controlled by the interaction of an aqueous metamorphic fluid, of low to moderate salinity, resulting in sub-micrometre depth scale isotopic modification at natural crystal faces and along penetrative micro-fracture networks, and that grain-scale isotopic modification was negligible. Therefore, we urge caution when considering regional chronological interpretations that appeal to significant zircon isotopic resetting caused exclusively by metamorphic fluid interaction at upper-amphibolite facies conditions. © 2002 Elsevier Science B.V. All rights reserved.

* Corresponding author. Present address: Geological Survey of Canada, 601 Booth St., Ottawa, ON, Canada K1A 0E8..
E-mail address: chris.carson@nrcan.gc.ca (C.J. Carson).

[1] Present address: Research School of Earth Sciences, Australian National University, Canberra, ACT 0200, Australia.

0012-821X/02/$ – see front matter © 2002 Elsevier Science B.V. All rights reserved.
PII: S0012-821X(02)00565-4

Keywords: zircon; fluid phase; U/Pb; ion probe; Napier Complex

1. Introduction

Zircon U–Pb geochronology has proven invaluable in assessment of the temporal evolution of numerous igneous and high-grade metamorphic terranes worldwide. In many cases, particularly in metamorphic rocks, U–Pb isotope systematics of zircon often exhibit significant departures from concordia. Proper understanding of the processes that generate discordance in natural settings, and the extent to which they operate, is necessary in order to correctly interpret isotope data and to assess the validity of concordia intercept ages [1,2].

Researchers have long recognised that mobilisation of radiogenic Pb (Pb*), and less commonly, U, from and within zircon can result in discordance [1–6]. Classic interpretations of U–Pb discordance emphasised both episodic Pb loss in response to younger geological events [3] and longer-term diffusive Pb* loss [4]. Experimental work, however, indicates that Pb diffusion within pristine crystalline zircon even at elevated temperatures is extremely lethargic which suggests that volume diffusion is unlikely to be the sole mechanism responsible for Pb* loss in most geological environments [7,8]. Hence, the current consensus is that for significant Pb* loss to occur in zircon, various additional factors, such as α-radiation damage, are important and often essential prerequisites [2,8–11].

Metamorphic fluids have been widely inferred to enhance mobility of Pb* in zircon, resulting in isotopic discordance [9,11,12]. Empirical studies confirm that, in the presence of hydrothermal fluids, mobility of Pb and, in some cases, U from zircon is a complex function of fluid composition, pressure, temperature, time and, particularly, the degree of radiation-induced lattice damage [9,13–15]. Based on conventional U–Pb zircon analysis and HF etching studies, Krogh and Davis [11] speculated that zircon alteration and Pb* loss was focussed along fractures and grain surfaces. They further proposed that zircon alteration and zircon discordance were strongly controlled by fluid interaction at the crystal surface and along penetrative fractures. Friend and Nutman [16] examined zircon behaviour during interaction with an assumed CO_2-rich granulite-facies metamorphic fluid in a field context and concluded that U–Pb systematics, in pristine to slightly damaged zircon, remained essentially unaffected. In contrast, Högdahl et al. [12] demonstrate that highly radiation damaged Palaeoproterozoic zircons almost completely lost accumulated Pb* during Caledonian-age low-temperature saline fluid interaction. Although other field studies imply that interaction with transient metamorphic fluids facilitates substantial Pb* loss in zircon resulting in partial to complete isotopic resetting [11,17–20], it is often difficult to confidently demonstrate the relationship of fluid infiltration with zircon isotopic modification. Furthermore, fluid compositions considered responsible for zircon modification in field settings are often uncertain. Isolating the effects of fluid interaction from other complicating factors such as deformation, which in the presence of fluids is known to facilitate Pb mobility [21], is also problematic. These uncertainties often necessitate extrapolation of well-defined empirical studies to the geological environment, as there are few field-based studies that explicitly examine zircon isotopic systematics with respect to fluids of known composition. This raises important issues. What is the magnitude, nature and length scale of zircon isotopic disturbance when exposed to infiltrating fluids, of known composition, under elevated metamorphic conditions in real geological environments?

In this contribution, we document an example of an Archaean orthogneiss which experienced fluid infiltration during the Early Palaeozoic. We show that introduction of an aqueous, low-salinity fluid, under static upper-amphibolite facies conditions, resulted in limited grain-scale isotopic disturbance of a pre-existing zircon population hosted within the orthogneiss. Furthermore, we propose that the observed isotopic disturbance is largely controlled by extensive isotopic resetting and/or recrystallisation along penetrative fracture

surfaces to depths on the sub-micrometre scale and by internal redistribution of Pb* enhanced by fracture-controlled fluid access.

2. Geological setting

The Napier Complex, east Antarctica (Fig. 1) experienced ultra-high-temperature regional metamorphism (UHT >1000°C) during the Archaean [22], conditions which effectively dehydrated the terrane. Southwestern areas of the complex, including Tonagh Island (the location of this study, Fig. 1), were subsequently dissected by narrow early Palaeozoic felsic pegmatite swarms [23,24] and associated parallel quartz veins. Adjacent to such pegmatites (Fig. 2), spectacular zones or selvedges of upper-amphibolite facies metasomatic alteration are common [23]. The alteration selvedges are the product of rehydration and recrystallisation of the host protolith as a result of fluid infiltration accompanying pegmatite emplacement. No pervasive deformation of the host lithology accompanied pegmatite emplacement or fluid infiltration. Tonagh Island, typical of the Napier Complex, is dominated by orthopyroxene-bearing felsic orthogneiss [25,26]. Within this host lithology, the alteration selvedge (samples 28/6, 28/1 and 28/2; Fig. 2) is characterised by replacement of UHT orthopyroxene by hornblende, biotite and epidote-bearing assemblages (see Appendix), resulting primarily from the addition of H_2O. In contrast, the protolith (sample 27; Fig. 2) witnessed only minor development of biotite and hornblende fringes on orthopyroxene and on ilmenite–magnetite pairs, indicating greatly reduced fluid interaction distal from the pegmatite. Comparison of zircons from relatively unaffected Archaean protolith and from zones of fluid–rock interaction adjacent to pegmatites permits detailed assessment of the physical and isotopic disturbance that might be experienced by zircon during upper-amphibolite facies fluid infiltration. Analysis of pegmatite equilibrium mineral assemblages permits pressure and temperature estimates during fluid infiltration to be determined together with fluid compositional information. This setting provides a tightly constrained field example where the effects of a fluid, of known composition, on zircon can be assessed and examined.

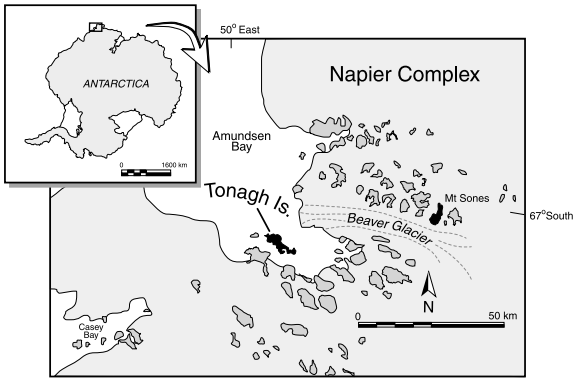

Fig. 1. Location of Tonagh Island (black) within Archaean Napier Complex (after Sheraton et al. [25]). Location of Mt Sones (discussed in text) is also shown (black). Inset: Location of Napier Complex within Antarctic continent.

3. Methods

3.1. Mineral compositions, imaging and P–T–fluid estimations

Mineral composition determinations and backscattered electron (BSE) imaging (Fig. 3) were done using the JEOL JXA-8600 electron microprobe located at Yale University, employing wavelength dispersive spectrometers, a range of natural and synthetic standards, and $\phi(\rho z)$ matrix corrections. Analytical conditions for all phases except zircon were 15 kV accelerating voltage, 15 nA beam current, a 10 μm beam spot for muscovite and biotite and a 5 μm beam spot for garnet and feldspars. A focussed beam ($\sim$2 μm) and 50 nA beam current were used for zircon. Pressure–temperature estimates were calculated using THERMOCALC v3.0 [27]. Biotite from the alteration selvedge and pegmatite were used to estimate $\log(a_{H2O}/a_{HCl^\circ})$, $\log(a_{H2O}/a_{HF^\circ})$ and HCl° and HF° molalities using the methods of Zhu and Sverjensky [28].

3.2. Crystal size distribution analysis

Crystal size distribution analysis [29] was con-

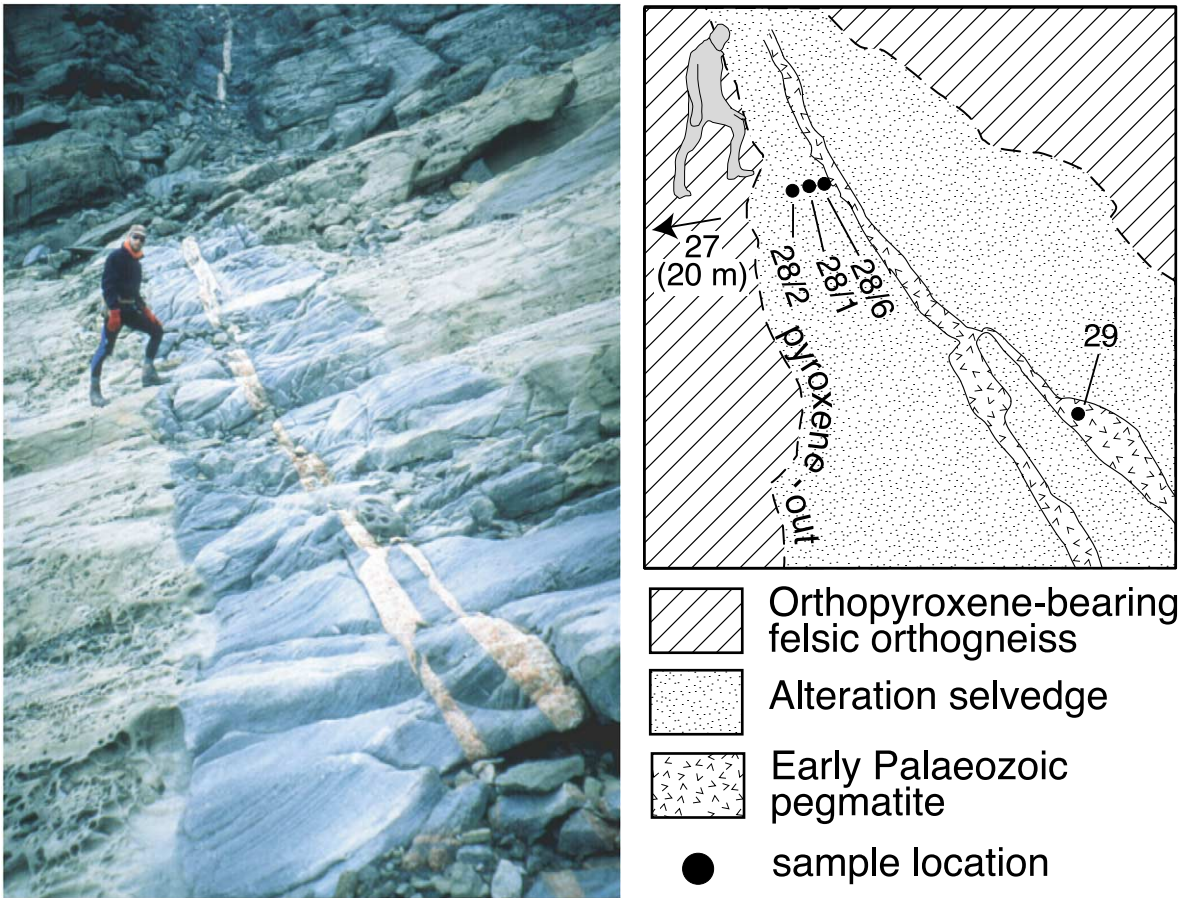

Fig. 2. Photograph and sketch map of alteration selvedge within Archaean orthopyroxene-bearing felsic orthogneiss adjacent to early Palaeozoic pegmatite, Tonagh Island, Napier Complex. Note conspicuous 'bleach' zone adjacent to pegmatite. The visible outer boundary of alteration selvedge indicates pyroxene-out isograd in host orthogneiss. Alteration selvedge cross-cuts UHT gneissosity and lithological contacts at high angle and clearly does not represent primary lithological features. Samples 28/6, 28/1 and 28/2 are 10 mm, 160 mm and 300 mm respectively from left margin of the pegmatite. Photographer facing east, geologist for scale, location lat. 67°05′37.3″S, long. 050°17′09.8″E.

ducted on in situ zircons from both altered and unaltered domains to assess the extent of physical dissolution or growth of zircon as a consequence of fluid interaction. Zircon short and long axis measurements were conducted optically using a petrographic microscope with an actuated *x-y* stage using a calibrated eye piece. Short axis measurements were used in the determination of crystal size distributions according to the methods of Peterson [29], where n = number of crystals per unit volume with length $\geq \mathbf{L}$, ($\mathbf{L} = L{\cdot}S$, S is a scaling factor to convert L which is a 2-D measurement of the short axis into an estimate of the 3-D short axis value, Fig. 4). As scaling is a function of crystal shape, we used a representative prism with axis dimensions, $a = 0.4$; $b = 0.4$; $c = 1$.

3.3. Ion microprobe U–Th–Pb analysis

Zircons were extracted using standard heavy liquid and magnetic techniques from both the protolith and hydrated selvedge (Fig. 2). Monazites were extracted from the pegmatite (sample 29) in a similar manner. No zircon was detected in the pegmatite. Zircon and monazite grains selected for conventional spot analysis were

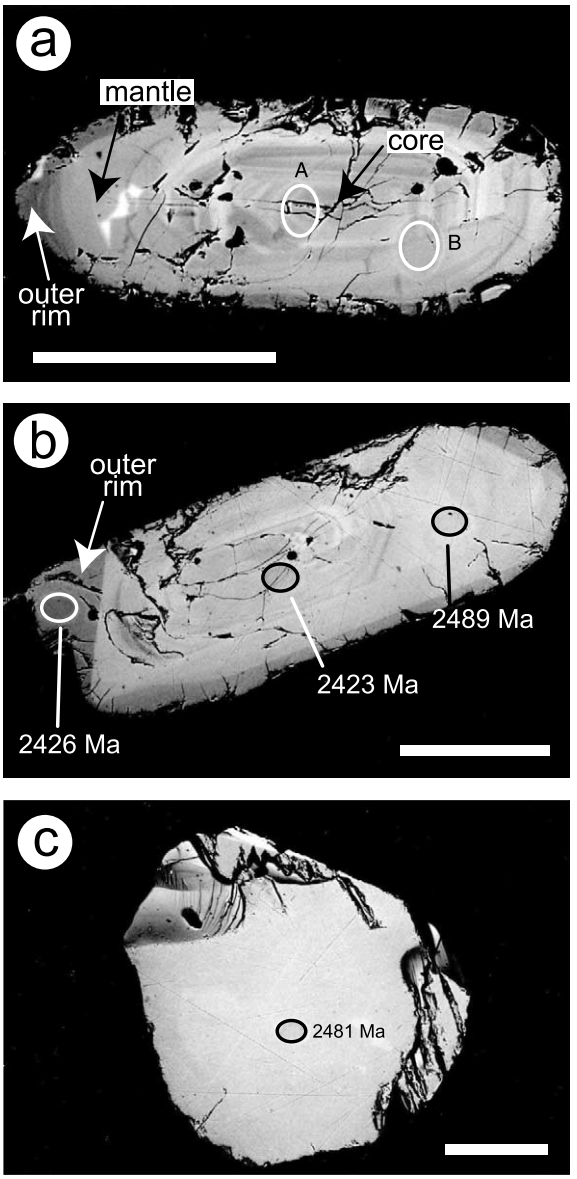

Fig. 3. BSE images of representative zircon morphologies. Annotated ages are $^{207}Pb/^{206}Pb$ ages; scale bar in all images = 100 μm. (a) Sample number 28/2, grain 3 (disc 1), note zoned ~2600 Ma core (labelled 'A'), overgrown by faintly zoned mantle (labelled) and outer rim (labelled). Analysis point 'B' (~2526 Ma) rejected due to overlap with significantly older core. (b) Sample 28/1, grain 5 (disc 7). Finely zoned core (reset to ~2423 Ma?) overgrown by mantle and outer rim (labelled), outer rim appears to truncate mantle. (c) Sample 28/6, grain 15 (disc 7). Homogeneous anhedral grain with negligible zoning.

mounted in epoxy together with standards, then sectioned, polished, and coated with Au. BSE imaging was conducted to assess internal zircon structure and to facilitate selection of analysis sites (Fig. 3).

Additional grains were selected for depth profiling measurements and epoxy-mounted such that morphologically identifiable crystal faces coincided with the analysis surface. The analysis surface was ultrasonically cleaned and Au-coated without further processing. Depth profiling measurements performed here differed from conventional spot analysis only in the sense that long-duration (~45 min) ion drilling was performed on unpolished grain boundaries to obtain a spatial record of U–Pb isotopic variation versus depth relative to natural crystal faces on the sub-micrometre to micrometre length scale.

U–Pb ion microprobe analyses on zircon, and U–Th–Pb analyses on monazite, were conducted using UCLA's CAMECA IMS 1270, and employing previously published analytical protocols [30,31]. Lead isotopic ratios were corrected using measured ^{204}Pb as proxy for common Pb. Relative sensitivity factors for U/Pb and Th/Pb were determined using AS-3 zircon and 554 monazite respectively. Data reduction and processing were performed using in-house UCLA software (ZIPS v2.4.1; C.D. Coath, 2000) and ISOPLOT v2.3 of Ludwig [32]. Uranium and Th concentrations were estimated semiquantitatively by comparing $U/^{94}Zr_2O$ and/or $Th/^{94}Zr_2O$ in the unknowns relative to values obtained from the standards [33]. Errors ellipses shown in Figs. 5–7 are at the 1σ level, whereas weighted mean and intercept ages are quoted at the 2σ level and include U decay constant uncertainties.

4. Results

4.1. P–T–fluid composition estimations

For H_2O-saturated conditions, average pressure–temperature estimates using the pegmatite assemblage (garnet, biotite, muscovite, K-feldspar, plagioclase and quartz; Table 1) are 8.1 kbar and 684°C. Fluid-absent calculations yield

8.0 kbar and 666°C. These results are identical at the 2σ level (minimum uncertainties ± ~30°C, ± ~1.5 kbar), suggesting that the infiltrating fluid was dominated by H_2O. This conclusion is also supported by the absence of calcite or other carbonate-bearing phases, either within the pegmatite or in the alteration selvedges. At these *P–T* conditions, $\log(a_{H2O}/a_{HCl^\circ})$ and $\log(a_{H2O}/a_{HF^\circ})$ values calculated for biotite from the hydrated zone are 2.9–3.2 and 2.4–2.7 respectively (Table 2). Values obtained from biotite from the pegmatite are 2.2–2.6 and 2.5–2.7 respectively. To estimate the molality of HCl° and HF°, we assumed an activity of H_2O of ~1, and that the activities of HCl° and HF° were approximately equal to their molalities (e.g., $a_{HCl^\circ} = \gamma m_{HCl^\circ}$ where the activity constant, γ, is ~1 for a neutral aqueous species). Estimates of HCl° and HF° molality range from 6 to 20×10^{-4} and 2 to 4×10^{-3}, respectively within the hydrated zone. These essentially overlap with molalities of HCl° and HF° calculated from the pegmatite biotites ($3–6\times10^{-3}$ and $\sim2.5\times10^{-3}$, respectively). These small molalities do not account for the total halogen budget of the fluid, but they clearly indicate a typical low- to moderate-salinity metamorphic fluid with low F content [28,34].

Table 1
Mineral compositions used in *P–T* estimates

	Sample 29 pegmatite				
	K-feldspar	plagioclase	garnet rim	muscovite	biotite
SiO_2	65.67	65.30	36.51	45.83	34.46
TiO_2	0.00	0.00	0.00	0.07	1.26
Al_2O_3	18.95	21.55	20.61	33.69	18.99
FeO[a]	0.02	0.02	32.24	2.81	25.90
MnO	0.00	0.00	7.42	0.00	0.13
MgO	0.00	0.00	1.56	0.59	5.53
CaO	0.29	2.66	1.27	0.01	0.01
Na_2O	2.92	10.00	0.00	0.43	0.00
K_2O	12.30	0.19	0.00	10.31	9.20
Total	100.15	99.72	99.61	93.75	95.48
Oxygens	8	8	12	22	22
Si	2.99	2.88	2.99	6.24	5.40
Ti	0.00	0.00	0.00	0.01	0.15
Al	1.02	1.12	1.99	5.41	3.51
Fe	0.00	0.00	2.21	0.32	3.40
Mn	0.00	0.00	0.52	0.00	0.02
Mg	0.00	0.00	0.19	0.12	1.29
Ca	0.01	0.13	0.11	0.00	0.00
Na	0.26	0.86	0.00	0.11	0.00
K	0.72	0.01	0.00	1.79	1.84
Sum	4.99	4.99	8.01	14.00	15.61

[a] All Fe as FeO.

4.2. Zircon morphology

Zircons from both the relatively unaltered and the hydrated protolith have similar morphologies. Most common are euhedral to subhedral, clear to honey-coloured grains, ~100 to ~250 μm in length, that have aspect ratios of ~2–3. Under BSE imaging, sectioned grains may exhibit fractured well-defined cores which may contain diffuse micrometre-scale oscillatory zoning (Fig. 3a,b). Typically, core regions are overgrown by a volumetrically dominant mantle, which, although generally homogeneous (Fig. 3a,b), may exhibit oscillatory zoning at the micrometre scale. The mantle may cross-cut the core regions (Fig. 3a) but more typically shows a conformable relationship with the cores. A narrow (< 20 μm), low-U rim (dark in BSE and bright in CL) is typically visible on many euhedral sectioned zircons (Fig. 3a) and may cross-cut delicate oscillatory zoning present in the mantle. Another major population consists of anhedral spherical glassy 'gem-like' pinkish grains (Fig. 3c; also described by Black et al. [35] from Mt Sones; Fig. 1), up to 20–500 μm in diameter, which display minimal structural development, and lack a clearly defined euhedral core or micrometre-scale oscillatory zoning, although some coarse (10–20 μm) zoning may be present.

Crystal size distribution analysis [29] results (presented in Table 3 and illustrated in Fig. 4) indicate that there is no statistically meaningful difference in the lengths of zircon short axes between the alteration selvedge (69.5 ± 6 μm; $n = 484$) and the protolith (69.6 ± 8 μm; $n = 143$). These results imply that: (1) there was minimal physical resorption or Ostwald ripening of zircon during fluid interaction; and (2) no *substantial*, micrometre-scale growth of early Palaeozoic zircon occurred either as rims on Palaeoproterozoic crystals or as new grains. Visual observations of in situ and mounted zircon grains support these assessments. Hence there is no indication that the infiltrating fluids caused grain-scale growth or dissolution modifications in zircon.

4.3. Pegmatite monazite U–Th–Pb ages

Weighted mean U–Pb (23 analyses) and Th–Pb (17 analyses) ages determined from 12 monazite grains from the pegmatite are identical within error (sample 29; Fig. 2). These include $^{206}Pb/^{238}U$, $^{207}Pb/^{235}U$, and $^{208}Pb/^{232}Th$ ages of 499.7 ± 3.4 Ma, 496 ± 2.9 Ma and 498 ± 1.7 Ma respectively (Table 4a,b; Fig. 5). Based on the criteria of [36], it is not valid to calculate a U–Pb concordia age from these data even though all estimates are identical at the 2σ level. Hence we simply accept the $^{208}Pb/^{232}Th$ age of 498 ± 1.7 Ma as the best estimate of the timing of pegmatite emplacement and fluid infiltration.

4.4. Zircon U–Pb systematics

4.4.1. Spot analysis results from sectioned grains

U–Pb analyses of sectioned zircons from the protolith and altered selvedge are presented on conventional concordia diagrams (Figs. 5 and 6) and tabulated in Tables 5 and 6. Oscillatory-zoned cores (Fig. 3a) occasionally record older

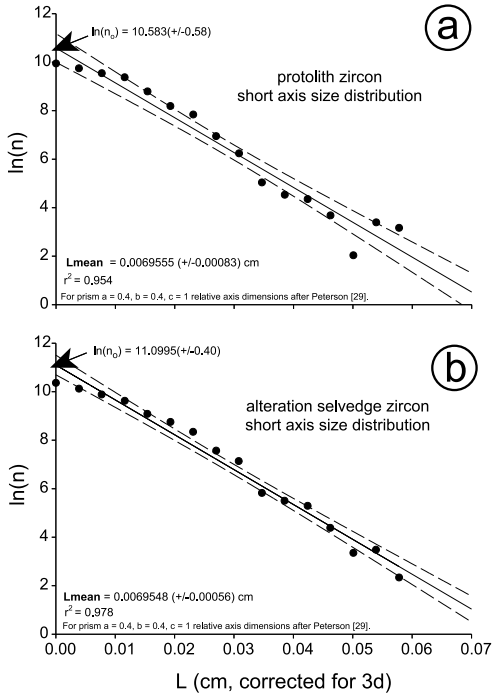

Fig. 4. (a) Short axis crystal size distribution diagrams (after [29]) for zircon populations from protolith, average grain size for this population is 69.6 ± 8 μm. (b) Alteration selvedge; average grain size for this population is 69.5 ± 6 μm. Error envelopes are at the 95% confidence limit.

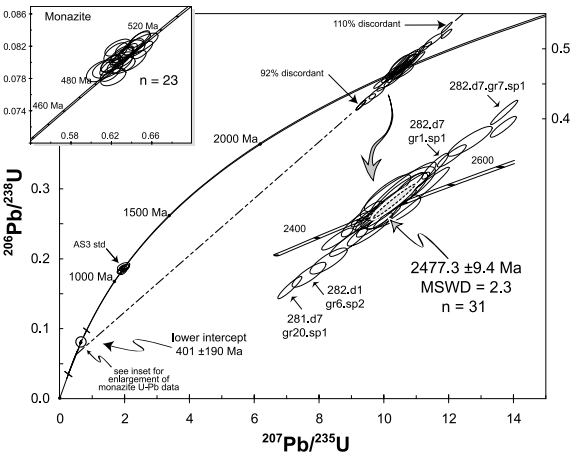

Fig. 5. Conventional concordia diagram showing zircon U–Pb isotope data from alteration selvedge. Regression line is an error-weighted regression with intercepts at 401 ± 190 Ma and 2477.3 ± 9.4 Ma. Monazite U–Pb data from pegmatite (sample 29) are plotted on concordia for reference (inset), but are not included in the lower intercept determination. Bootstrap average of U–Pb data is indicated by the dashed grey ellipse in the enlargement of the zircon data. Selected zircons arrowed and discussed in text.

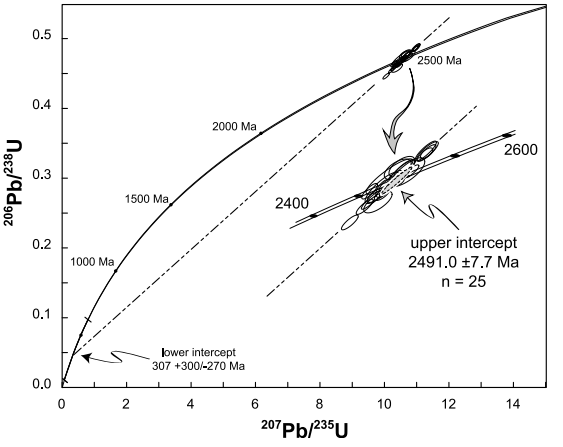

Fig. 6. Conventional concordia diagram showing zircon U–Pb isotope data from protolith. Regression line is an error-weighted regression with intercepts at $307^{+300}/_{-270}$ Ma and 2491.0 ± 7.7 Ma. Bootstrap average of U–Pb data is indicated by the dashed grey ellipse in the enlargement of the zircon data. Selected zircons arrowed and discussed in text.

ages (>2600 Ma). The details, isotopic data and regional implications of these older cores will be presented elsewhere.

4.4.1.1. Alteration selvedge

In total, 31 analysis sites were investigated on 23 zircon grains from the alteration selvedge. Analyses were generally obtained from the relatively unstructured, volumetrically dominant mantle regions (Fig. 3a,b), but also include cores. The latter generally exhibit elevated U contents with similar $^{207}Pb/^{206}Pb$ ages to those of the metamorphic mantles. Fig. 5 illustrates the spot zircon U–Pb analyses from the alteration selvedge, together with U–Pb data for monazites from the pegmatite. Uranium contents, while typically moderate (~400–700 ppm), were as high as ~2200 ppm in core regions. Thorium contents varied between ~100 and 400 ppm but reached ~1500 ppm in core regions. An important aspect of the isotopic data for zircon presented in Fig. 5 is the spread of discordance, ranging from ~92% normal to ~110% reverse discordance (individual concordance calculated after [15]). Based upon the statistical criteria of Ludwig [36], these data do not represent a concordant population, therefore a concordia age cannot be calculated. However, an error-weighted regression [32] performed using these zircon data yielded an upper intercept age of 2477.3 ± 9.4 Ma with an imprecise lower intercept age of 401 ± 190 Ma ($n = 31$, MSWD = 2.3). A bootstrap statistical analysis [37] of these data from the alteration selvedge is indicated by the dashed ellipse (Fig. 5) that represents the 2σ uncertainty on the pooled average.

Table 2
Biotite analyses used in HCl° and HF° calculations

	Wall rock biotite				Pegmatite biotite	
	28/5	28/5	28/6	28/6	29	29
SiO_2	35.60	35.54	35.44	35.13	34.36	34.62
TiO_2	4.82	4.37	4.19	4.33	1.64	1.80
Al_2O_3	14.62	14.27	14.95	14.87	18.38	18.68
FeO[a]	22.95	24.70	24.31	24.12	26.04	26.20
MnO	0.47	0.42	0.51	0.48	0.10	0.08
MgO	8.01	7.79	7.38	7.22	5.67	5.26
CaO	0.06	0.05	0.08	0.06	0.01	0.00
BaO	0.28	0.27	0.33	0.26	0.01	0.05
Na_2O	0.06	0.09	0.06	0.04	0.07	0.04
K_2O	9.23	9.12	9.31	9.24	9.13	9.27
F	0.16	0.26	0.24	0.19	0.122	0.095
Cl	0.01	0.02	0.03	0.04	0.184	0.209
(O = Cl, F)	−0.07	−0.11	−0.11	−0.09	−0.09	−0.09
H_2O[b]	3.86	3.82	3.83	3.83	3.83	3.83
Total	100.05	100.60	100.57	99.71	99.44	100.04
Si	5.06	5.08	5.07	5.05	4.96	4.97
Ti	0.52	0.46	0.45	0.47	0.18	0.19
Al	2.45	2.41	2.52	2.52	3.13	3.16
Fe	2.73	2.95	2.91	2.90	3.15	3.15
Mn	0.06	0.05	0.06	0.06	0.01	0.01
Mg	1.70	1.66	1.57	1.55	1.22	1.13
Ca	0.01	0.01	0.01	0.01	0.00	0.00
Ba	0.02	0.02	0.02	0.02	0.00	0.00
Na	0.02	0.03	0.02	0.01	0.02	0.01
K	1.68	1.66	1.70	1.70	1.68	1.70
F	0.070	0.117	0.110	0.087	0.056	0.045
Cl	0.003	0.004	0.007	0.009	0.045	0.051
OH	3.665	3.644	3.647	3.677	3.687	3.665

Structural formulas based on 22 oxygens.
[a] All Fe as FeO.
[b] H_2O estimated based on oxygen stoichiometry.

4.4.1.2. Protolith

Zircon U–Pb analyses from the anhydrous protolith consisted of 25 analyses from 15 zircon grains, primarily from unstructured metamorphic mantles (Fig. 3a,b) and anhedral grains (Fig. 3c) with generally elevated Th/U. Uranium contents are typically ~300–600 ppm and Th contents ~400–900 ppm. When compared to the zircon results from the hydrated zone, analyses from the protolith show a reduced spread of discordance. The data yield an upper intercept age of 2491.0 ± 7.7 Ma and an imprecise lower intercept of $307^{+300}/_{-270}$ Ma ($n = 25$, Monte Carlo regression; Fig. 6). A bootstrap analysis of these data from the unaltered protolith is indicated by the dashed ellipse (Fig. 6), representing the 2σ uncertainty on the pooled average. The lower intercept, while highly imprecise, is within 2σ of the value obtained from zircons from the alteration selvedge.

4.4.2. Ion drilling results from unpolished natural crystal faces

U–Pb depth profiling of a single zircon from the alteration selvedge (sample 28/6) is presented on a conventional concordia diagram (Fig. 7a) and tabulated in Table 7a,b. In order to assess

Table 3
Zircon crystal size distribution data

Zircons from alteration selvedge		Zircons from protolith	
size fraction (μm)	No. of crystals	size fraction (μm)	No. of crystals
0–24	5	0–24	7
25–29	2	25–29	0
30–34	23	30–34	10
35–39	12	35–39	7
40–45	53	40–45	14
45–50	9	45–50	6
50–55	70	50–55	29
55–60	14	55–60	4
60–65	50	60–65	14
65–70	11	65–70	0
70–75	55	70–75	9
75–80	10	75–80	7
80–85	50	80–85	11
85–90	5	85–90	1
90–95	25	90–95	9
95–100	2	95–100	0
100–105	38	100–105	3
105–110	1	105–110	2
110–120	12	110–120	3
120–125	11	120–125	2
125–130	1	125–130	0
130–135	4	130–135	1
135–140	1	135–140	0
140–150	2	140–150	0
150–160	8	150–160	1
160–170	4	160–170	1
170–200	2	170–200	0
200–210	3	200–210	1
>210	1	>210	1
Total	**484**	Total	**143**
Total area	**255.8085 cm^2**	Total area	**100.3580 cm^2**

changing isotopic information with respect to depth relative to the crystal surface, these data are presented as single cycle analyses. It should be stressed that when interpreting depth profiling data, the uncertainties on single cycle analyses are individually larger than would be obtained on a statistically pooled mean on an isotopically homogeneous analysis site. However, despite this reduced precision, valuable near-surface isotopic information, as a function of depth, can be obtained. Two depth profile runs are presented, the first (Table 7a, total number of cycles = 14, no rejections) was conducted on a pre-sputtered surface (120 s). Pre-sputtering was initially conducted in order to 'clean' surface contamination and to remove the conductive Au coat. The second depth profile run (Table 7b, total number of cycles = 40, 32 analyses accepted; several deeper analyses were rejected due to sample charging and decreasing analytical precision) was conducted on a non-pre-sputtered surface. Pit depths were measured using a profilometer and, based on cumulative analytical run times, a calibration of the sputter rate was determined to be 0.56–0.85 μm/h (average 0.71 μm/h) for the depth profiling session analytical conditions.

Fig. 7 shows the combined results from the pre-sputtered and non-pre-sputtered depth profiles. A relatively simple, near concordant, population of ages is obtained from the pre-sputtered analysis (28/6.6.2.1), yielding a concordia age [36] of 1806 ± 34 Ma, strongly suggesting a period of zircon growth, or of complete isotopic resetting, at this time. In contrast, the non-pre-sputtered depth profile (28/6.6.2.3) illustrates that the very near-surface zircon (0 to ~0.06 μm, Fig. 7b) shows near complete resetting at ~500–700 Ma (lower intercept 608 ± 77 Ma) with a Th/U ~0.1 and an elevated U content (~1000 ppm). With increasing depth, individual analyses progressively track along a chord toward a upper intercept of 1931 ± 56 Ma with generally decreasing U contents (to ~150 ppm) and increasing Th/U, to a maximum analysis depth of ~0.5 μm. This upper intercept broadly correlates with zircon having a concordia age of 1806 ± 34 Ma derived from analysis 28/6.6.2.1. If these two data sets are regressed together (Fig. 7a) a lower intercept of 558 ± 75 Ma and an upper intercept of 1882 ± 41 are obtained, with no excess scatter (MSWD = 0.92). Fig. 7b illustrates an important point in that the depth scale of significant zircon modification at ~500 Ma is small, at around 0.06 μm.

It should be noted that an U–Pb zircon age of ~1800 Ma has not been previously documented from the Napier Complex. In situ ion probe Th–Pb ages on monazite from the protolith (as mantles on pre-existing apatite; Carson and Ague, unpublished data) and several chemical Th–U–total Pb isochron ages from monazite and xenotime elsewhere within the Napier Complex [38,39] provide independent confirmation of an isotopic disturbance at about this time. The geological signifi-

Table 4a
Monazite U–Pb isotope results

Age (Ma)						% Radiogenic $^{206}Pb^{*b}$	Corrected atomic ratios						Date\ sample#.grain#.spot#
$\frac{^{206}Pb}{^{238}U}$	±[a]	$\frac{^{207}Pb}{^{235}U}$	±	$\frac{^{207}Pb}{^{206}Pb}$	±		$\frac{^{207}Pb^*}{^{235}U}$	±	$\frac{^{206}Pb^*}{^{238}U}$	±	$\frac{^{207}Pb^*}{^{206}Pb^*}$	±	
494.6	4.10	496.6	4.06	505.6	15.2	99.6	0.6307	0.00652	0.07974	0.00069	0.05737	0.000395	2000-07Sept\ 29.gr10.sp1
497.4	4.92	503.7	4.93	532.2	18.7	99.5	0.6423	0.00798	0.08022	0.00082	0.05806	0.000496	2000-07Sept\ 29.gr10.sp2
506.2	4.35	501.4	5.97	479.8	31.1	99.3	0.6386	0.00963	0.08168	0.00073	0.05670	0.000798	2000-07Sept\ 29.gr11.sp1
493.1	4.23	489.1	4.28	470.5	16.1	99.4	0.6188	0.00682	0.07949	0.00071	0.05646	0.000410	2000-07Sept\ 29.gr11.sp2
507.6	3.95	503.1	4.32	482.5	18.3	99.6	0.6413	0.00699	0.08193	0.00066	0.05677	0.000471	2000-07Sept\ 29.gr12.sp1
513.1	4.20	506.9	4.28	478.7	15.5	99.6	0.6474	0.00694	0.08285	0.00071	0.05667	0.000398	2000-07Sept\ 29.gr1.sp1
503.6	4.28	499.8	3.97	482.6	15.5	99.7	0.6360	0.00639	0.08125	0.00072	0.05677	0.000399	2000-07Sept\ 29.gr3.sp1
502.1	4.09	496.2	4.48	469.1	19.2	99.5	0.6302	0.00719	0.08101	0.00069	0.05642	0.000489	2000-07Sept\ 29.gr3.sp2
495.2	4.28	490.1	4.36	466.3	21.7	99.6	0.6203	0.00696	0.07984	0.00072	0.05635	0.000553	2000-07Sept\ 29.gr4.sp1
500.7	4.19	496.0	4.73	473.9	19.3	99.5	0.6298	0.00760	0.08078	0.00070	0.05655	0.000493	2000-07Sept\ 29.gr4.sp2
503.4	4.80	492.6	4.85	442.6	22.1	99.4	0.6243	0.00776	0.08121	0.00080	0.05575	0.000555	2000-07Sept\ 29.gr5.sp1
495.3	4.02	489.4	4.09	461.7	17.7	99.5	0.6192	0.00652	0.07986	0.00067	0.05624	0.000449	2000-07Sept\ 29.gr6.sp1
517.2	5.29	522.3	12.80	544.5	60.2	97.4	0.6726	0.02110	0.08354	0.00089	0.05839	0.001610	2000-07Sept\ 29.gr6.sp2
505.8	4.14	505.5	4.35	503.9	17.9	99.5	0.6451	0.00706	0.08162	0.00069	0.05732	0.000467	2000-07Sept\ 29.gr7.sp1
500.6	5.05	497.1	4.29	481.3	17.1	99.6	0.6317	0.00690	0.08075	0.00085	0.05674	0.000439	2000-07Sept\ 29.gr7.sp2
491.6	4.68	487.5	6.22	468.5	31.3	99.5	0.6163	0.00990	0.07924	0.00078	0.05641	0.000799	2000-07Sept\ 29.gr8.sp1
494.0	4.16	495.9	5.70	504.4	28.7	99.4	0.6296	0.00914	0.07965	0.00070	0.05733	0.000747	2000-07Sept\ 29.gr9.sp2
509.5	5.44	507.8	7.09	500.1	25.8	99.6	0.6488	0.01150	0.08224	0.00091	0.05722	0.000670	2000-07Sept\ 29.gr1.sp2
498.0	3.89	496.5	4.69	489.4	21.5	99.4	0.6306	0.00752	0.08031	0.00065	0.05695	0.000555	2000-07Sept\ 29.gr2.sp1
488.1	3.96	489.2	4.13	494.6	18.6	99.6	0.6190	0.00659	0.07865	0.00066	0.05708	0.000482	2000-07Sept\ 29.gr12.sp2
507.0	4.13	493.7	5.23	432.5	23.3	99.4	0.6262	0.00837	0.08183	0.00069	0.05550	0.000581	2000-07Sept\ 29.gr9.sp1
485.3	4.23	491.0	5.17	518.1	24.9	99.5	0.6219	0.00825	0.07818	0.00071	0.05769	0.000655	2000-07Sept\ 29.gr5.sp2
489.8	5.28	483.4	6.00	453.1	30.3	99.4	0.6097	0.00952	0.07894	0.00088	0.05602	0.000765	2000-07Sept\ 29.gr2.sp2

[a] Uncertainties listed at the 1σ level.
[b] Correction for common Pb made using the measured $^{204}Pb/^{206}Pb$ ratio.

Table 4b
Monazite Th–Pb isotope results

Age (Ma)				% Radiogenic $^{208}Pb^{*}$ [b]	Date\ sample#.grain#.spot#
$^{208}Pb/^{232}Th$	± [a]	$^{208}Pb/^{232}Th$	±		
502.4	3.10	0.0252	0.00016	99.7	2000-07Sept\ 29.gr10.sp1
498.8	3.24	0.0250	0.00016	99.6	2000-07Sept\ 29.gr10.sp2
496.9	2.48	0.0249	0.00013	99.8	2000-07Sept\ 29.gr11.sp1
500.7	2.80	0.0251	0.00014	99.6	2000-07Sept\ 29.gr11.sp2
503.5	2.55	0.0252	0.00013	99.7	2000-07Sept\ 29.gr12.sp1
501.9	2.54	0.0251	0.00013	99.7	2000-07Sept\ 29.gr1.sp1
498.1	2.43	0.0250	0.00012	99.8	2000-07Sept\ 29.gr3.sp1
499.8	2.68	0.0250	0.00014	99.8	2000-07Sept\ 29.gr3.sp2
499.5	2.76	0.0250	0.00014	99.8	2000-07Sept\ 29.gr4.sp1
494.2	2.74	0.0248	0.00014	99.8	2000-07Sept\ 29.gr4.sp2
498.6	2.55	0.0250	0.00013	99.7	2000-07Sept\ 29.gr5.sp1
497.0	2.65	0.0249	0.00013	99.8	2000-07Sept\ 29.gr6.sp1
500.9	2.91	0.0251	0.00015	98.6	2000-07Sept\ 29.gr6.sp2
500.7	2.84	0.0251	0.00014	99.7	2000-07Sept\ 29.gr7.sp1
486.1	4.98	0.0243	0.00025	99.8	2000-07Sept\ 29.gr7.sp2
500.0	3.20	0.0251	0.00016	99.8	2000-07Sept\ 29.gr8.sp1
492.8	3.26	0.0247	0.00017	99.8	2000-07Sept\ 29.gr9.sp2

[a] Uncertainties listed at the 1σ level.
[b] Correction for common Pb made using the measured $^{204}Pb/^{208}Pb$ ratio.

cance of this isotopic 'event' remains speculative. However, for the purposes of this contribution, the important issue is that the very near-surface zircon was profoundly affected at ~500 Ma (to a depth of ~0.06 μm) and the age and geological significance of the sub-surface zircon (~1800 Ma) is not particularly relevant. Further discussion of the significance of the ~1800 Ma age will be addressed elsewhere.

5. Discussion

5.1. Spatial extent of disturbed U–Pb systematics in zircon during fluid infiltration

The ion probe depth-profiling technique, when applied to natural crystal surfaces, provides a powerful means to assess the near-surface isotopic composition of zircon at a far higher spatial resolution than that possible with conventional ion probe analysis of sectioned grains. In this case, the method provides fundamental information regarding the depth scale of isotopic modification or zircon recrystallisation on surfaces exposed to infiltrating aqueous fluids during upper-amphibolite facies conditions. These results indicate (Fig. 7a,b) that near-complete isotopic resetting (or growth of a sub-micrometre-scale film of new zircon) was observed at the near surface (0–0.06 μm) and depth scale of 'modified' zircon with respect to the crystal surface is of the order of ~0.20–0.25 μm (Fig. 7b).

Krogh and Davis [11] demonstrated that zircon can exhibit high solubility (during HF exposure) along internal fractures and grain boundaries, and concluded that such domains are susceptible to alteration by fluid interaction. Furthermore, they concluded that zircon discordance is strongly correlated with the presence of such alteration domains. Air abrasion techniques [40] seek to eliminate potentially altered fractured zircon grains and suspect surface layers, resulting in whole grain zircon dissolution U–Pb ages that are considerably more concordant and displaced toward the upper intercept. It was surmised from these observations that outer layers of zircon and internal micro-fractures were loci of preferential Pb* loss [11,40]. The techniques then available did not permit direct isotopic measurement of zircon

grain surfaces and such conclusions were based on the response of the U–Pb system after removal of the material thought to be affected by Pb* loss. By conducting ion probe depth profiling of natural zircon crystal surfaces, we provide the first known *direct* isotopic measurement of the material that would be removed during air abrasion zircon preparation [40], and show that such material can provide valuable geological information. We further elaborate on the potential significance of these findings below (Section 5.3).

5.2. Significance of the normal and reverse discordance revealed in conventional spot analysis

Uranium–lead analysis of sectioned zircons from the alteration selvedge display a spread of reverse and normal discordance (92–110%), distributed about concordia, along a discord that has a lower intercept of 401 ± 190 Ma (Fig. 5). Zircon analyses from the protolith (Fig. 6) display similar though less pronounced behaviour. Upper intercept ages from the alteration selvedge (2477.3 ± 9.4 Ma) and the comparatively unaltered protolith (2491.0 ± 7.7 Ma) are identical at the 2σ level. We interpret these results to record a Palaeoproterozoic episode of zircon growth and/or extensive isotopic disturbance that has been previously reported in isotopic studies throughout the Napier Complex (e.g. [35]). Although a lower intercept age based exclusively on the zircon data from the alteration selvedge is imprecise (401 ± 190 Ma), pointing to disturbance near the Proterozoic–Palaeozoic boundary, the timing of pegmatite emplacement and aqueous fluid influx has been independently established at 498 ± 1.7 Ma. It is logical to conclude that the lower intercept recorded by the discordant zircon data developed in response to this event at ~500 Ma during which elevated metamorphic conditions (8 kbar and 675°C) prevailed.

We believe that the observed normal and reverse discordance is a geologically meaningful feature on the basis of the following: (1) the number of discordant analyses from the altered domain exceeds the number expected beyond 2σ of the mean, assuming a normal distribution for a concordant population, suggesting that the discordance cannot be accounted for by scatter due to experimental uncertainty alone; (2) analyses from both standard and unknown zircons define a similar range of UO^+/U^+ values minimising potential

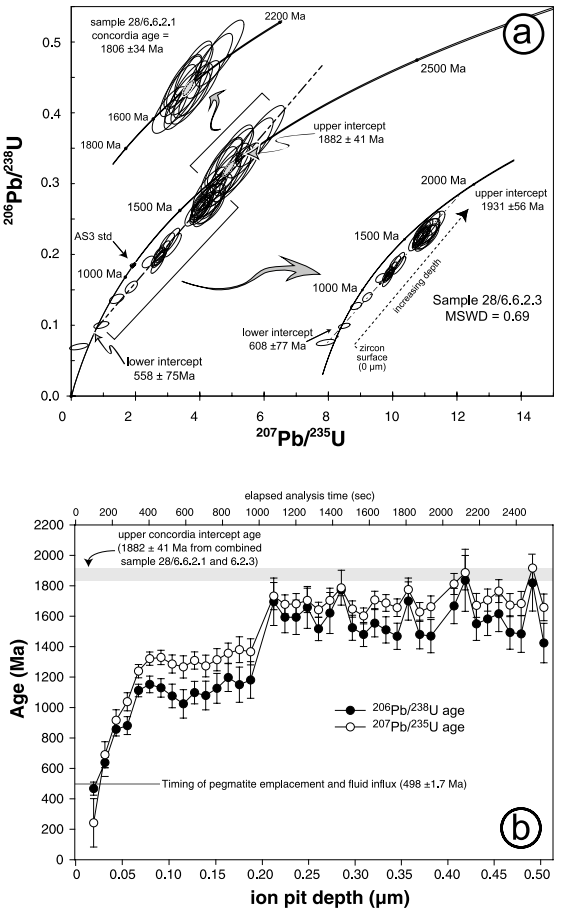

Fig. 7. (a) Conventional concordia diagram showing zircon U–Pb isotope data from depth profiling on zircon from sample 28/6. Regression line is an error-weighted regression with intercepts at 558 ± 75 Ma and 1882 ± 41 Ma, using combined data from analyses 28/6.6.2.1 and 28/6.6.2.3. Individual results are shown as enlargements; upper left, analysis 28/6.6.2.1 (pre-sputtered analysis site), has a concordia age of 1806 ± 34 Ma; lower right, analysis 28/6.6.2.3 (no pre-sputter prior to analysis), shows a discordant array from 608 ± 77 Ma to 1931 ± 56 Ma. (b) Age (Ma) versus analytical ion probe pit depth (µm) relative to zircon crystal surface calculated using a mean sputter rate of 0.71 µm/h. Measured elapsed analysis time (s) shown on upper scale. Individual single cycle $^{206}Pb^*/^{238}U$ and $^{207}Pb^*/^{235}U$ ages shown, error bars are 1σ. Note that the maximum depth of zircon significantly modified at ~500 Ma is ~0.20–0.25 µm.

bias produced by an inappropriate UO^+/U^+ vs Pb^+/U^+ calibration of Pb/U relative sensitivity; and (3) the moderate U contents associated with discordant results from the mantle region appear too low to produce the structural damage required to cause discordance simply by producing differential ionisation efficiencies of Pb and U relative to the standard [41–43]. While this latter consideration appears potentially applicable to the relatively 'high-U' cores, we wish to emphasise that the lower intercept indicated by our results coincides with a known geological episode, which seems to rule out such an effect. Specifically, discordance resulting from differential sputtering efficiency of Pb and U relative to the standard will produce a chord that extends through the origin [42,43].

Normal discordance observed in U–Pb studies of zircon is commonly attributed to either some degree of open system behaviour, typically partial Pb* loss from the zircon due to geological disturbance, or, as is sometimes the case with whole grain dissolution isotopic techniques, the physical mixing of an older zircon component with a younger overgrowth. Zircon discordance can also be generated by open system behaviour of U. Although U mobility has been documented in several experimental studies on zircon (e.g. [8,13]), in general, data on the open system behaviour of U within pristine and metamict zircon are sparse (e.g. [44]), and, where available, suggest that U mobility is up to four orders of magnitude less than that of Pb (e.g. [8]) under similar conditions. Whilst acknowledging that U open system behaviour can potentially contribute to the development of zircon U–Pb discordance, we maintain, in the following discussion, that open system Pb behaviour will be the primary contributor to the development of zircon discordance.

Reverse discordance has been subject to considerable debate. In their review of reverse discordance in both conventional and ion probe U–Pb studies of natural zircon, Mattinson et al. [6] differentiated between two scenarios to account for reverse discordance in zircon, one representing a real physical phenomenon, the other, the result of the analytical artefacts which we have eliminated as possibilities. The first focuses on the internal intra-grain redistribution of Pb* from 'high-U domains' to 'low-U domains' within the zircon, resulting in localised net Pb* excess, a term coined 'internal reverse discordance' [6]. This process was well illustrated in a detailed ion probe study by Williams et al. [5] who concluded that the extreme (up to ~150%) reverse (and normal) discordance exhibited by a single 3950 Ma zircon from Mt Sones in the Napier Complex (Fig. 1) was due to localised net Pb* gain (or loss) within the zircon at the sub-micrometre scale. This conclusion was based primarily on unusual fluctuations in Pb count rates during analysis acquisition which were not mirrored by variations in U or Th. Williams et al. [5] also noted a direct correlation in Pb/U ages with $^{207}Pb/^{206}Pb$ ages, the detection of which was greatly facilitated by the extreme discordance observed and by the relatively old lower intercept (~2000 Ma), effectively resulting in greater 'separation' of Pb/Pb and Pb/U ages along the discordant array. It should be stressed that extent of discordance under discussion here is far smaller (92–110%) than that reported by Williams et al. [5] and this, combined with a Early Palaeozoic lower intercept, renders detection of correlation between Pb/U and Pb/Pb ages difficult at best.

Nevertheless, we have detected significant compositional (and potential isotopic) heterogeneity within or adjacent to the ion probe analysis sites of our zircons using BSE imaging and wavelength dispersive electron probe analysis. Fig. 8a–d shows BSE images of three fractured, relatively high-U cores. Although the ion probe analysis sites shown in Fig. 8a–d are near concordant, fracture-controlled(?) compositional heterogeneity is clearly evident on the 1–10 μm scale. Electron probe analysis of the distinct semicontinuous, localised, 'bright' regions indicate that they contain ~3000–6000 ppm U, ~3000 ppm Pb and ~500–5000 ppm Th with Th/U values comparable or identical to those obtained by ion probe. In contrast, the 'darker' areas have far lower U, Th and Pb contents that are at or below detection limits (estimated at ~190, ~190 and ~500 ppm, U, Th and Pb respectively; J. Eckert, personal communication). The apparent relationship between internal fractures and localised regions of elevated U and Pb (Fig. 8a–d) and the highly ir-

regular distribution of such regions clearly suggest these features formed after zircon crystallisation.

Lee and Tromp [45] concluded that characteristic patterns of radial and concentric fractures in zircon that are similar to those we observe are due to self-induced volume expansion of radiation-damaged domains. The fractures shown in core regions and the radial fractures in outer regions (Fig. 8a–d) probably resulted from such a fracturing mechanism. Lee and Tromp [45] also concluded that U and Pb susceptibility to remobilisation from fractured domains is substantially enhanced by increased permeability and efficient fluid access to zircon interiors. Enhanced fluid access and fluid-mediated Pb and U diffusion along penetrative micro-fractures, acting together with thermal annealing processes, affecting structurally damaged areas [44] may account for the observed irregular distribution of U and Pb within zircon, shown in Fig. 8a–d. Whilst these observations and results do not conclusively indicate decoupling of uranogenic Pb from its parent within domains of fracture-related U and Pb enrichment, any remobilisation of U and Pb conceivably would present a potential opportunity for decoupling and for the development of significant discordance on a sub-micrometre scale.

A number of reverse and normal discordant analyses (Table 5) are from such fractured, relatively 'high-U' cores ($\sim$800–2200 ppm U), implying correlation between U content and degree of discordance (Table 5). Whilst this relationship is not always observed, it does support the general contention that enhanced Pb redistribution may be facilitated by increased structural damage, fluid access and localised thermal annealing [2,44,45] during fluid-saturated upper-amphibolite facies metamorphism. It should noted, however, that several ion probe sites that display marked discordance display no readily apparent fracture-controlled compositional heterogeneity (Fig. 8e,f).

5.3. Interpretation of U–Pb systematics

The spread of discordance illustrated by the zircon population in Figs. 5 and 6 resulted from disturbance during a much younger event ($\sim$500 Ma) than that in the case described by Williams et al. [5] from Mt Sones (Fig. 1). As the lower intercept for the normal and reversely discordant data presented in Figs. 5 and 6 is non-zero and coincides with a real geological event, we concluded above that the observed reverse discordance is genuine and not an analytical artefact. What process or mechanism may have produced the observed spread of discordance in the sectioned zircon (Figs. 5 and 6)? Published diffusion coefficients for Pb in gem-quality zircon [7,8] imply that at temperatures around 675°C, wholesale volume diffusion of Pb* in pristine zircon would be insufficient to account for localised net gain or loss of Pb* across the length scale of the ion beam analysis site (20–30 μm diameter). As highlighted previously, micro-fractures, lattice dislocations and other crystal defects, α-radiation damage, especially in the presence of metamorphic fluids, have been widely suggested to greatly enhance Pb diffusion within zircon, and these factors might contribute to isotopic discordance [7–15,44–46]. Depth profiling results (Fig. 7) indicate that significant isotopic disturbance, or growth of a sub-micrometre-scale film of new zircon, was restricted to $\sim$0.20–0.25 μm depth with respect to the crystal surface, and near complete resetting was observed only at the extreme near-surface (0–0.06 μm) environment. These observations provide a suitable proxy for assessing the degree of isotopic disturbance that might exist along penetrative micro-fractures observed within analysed zircons. If the presence of strongly reset or new zircon of $\sim$500 Ma age is common along surfaces exposed to the infiltrating metamorphic fluid, such as penetrating micro-fracture networks, normal discordance, as indicated in Figs. 5 and 6, may represent an analytical mixture of reset or new zircon along micro-fractures with adjacent unaffected zircon, which is schematically illustrated in Fig. 9b. Similarly, reverse discordance may be attributed to internal Pb* redistribution with localised enrichment of Pb* [5,6], on the micrometre to sub-micrometre scale, facilitated by fluid-enhanced diffusion along internal micro-fracture networks and annealing of radiation damaged domains (Fig. 9b). The inference of fracture networks controlling internal Pb (and U) redistribution (Fig. 8a–d) within core regions during

Table 5
Zircon U–Pb isotope data from alteration selvedge

Ages (Ma)						% radiogenic $^{206}Pb^{*b}$	Corrected atomic ratios						Th/U[c]	Disc. %[d]	U[e]	Th[e]	Date\ sample#.disc#.grain#.spot#
$^{206}Pb/^{238}U$	±[a]	$^{207}Pb/^{235}U$	±	$^{207}Pb/^{206}Pb$	±		$^{207}Pb^*/^{235}U$	±	$^{206}Pb^*/^{238}U$	±	$^{207}Pb^*/^{206}Pb^*$	±			(ppm)	(ppm)	
2495	29.3	2483	16.4	2474	14.2	99.5	10.54	0.187	0.4727	0.00670	0.1617	0.00136	0.5	100.8	538	270	2000-2Dec\\ 281.d1.gr12.sp2
2470	30.8	2470	17.5	2470	15.9	99.5	10.39	0.197	0.4668	0.00701	0.1614	0.00152	0.5	100.0	634	325	2000-2Dec\ 281.d1.gr15.sp3
2476	31.9	2485	21.9	2493	25.9	99.1	10.56	0.249	0.4682	0.00727	0.1636	0.00251	0.3	99.3	410	131	2000-2Dec\ 281.d1.gr16.sp2
2398	20.9	2424	12.1	2446	10.1	99.6	9.89	0.130	0.4506	0.00471	0.1591	0.00095	0.1	98.0	1047	120	2000-2Dec\ 281.d1.gr3.sp1
2335	25.0	2414	14.6	2481	14.9	99.4	9.78	0.155	0.4365	0.00558	0.1624	0.00144	0.1	94.1	492	58	2000-2Dec\ 281.d1.gr3.sp3r
2469	24.2	2459	11.8	2450	10.3	99.1	10.26	0.131	0.4668	0.00551	0.1594	0.00097	0.3	100.8	902	331	2000-2Dec\ 281.d1.gr3.sp4
2528	34.2	2482	17.0	2443	16.4	99.4	10.52	0.193	0.4803	0.00785	0.1588	0.00154	0.5	103.5	485	243	2000-2Dec\ 281.d1.gr8.sp2
2295	24.1	2390	13.6	2473	13.3	99.6	9.53	0.141	0.4276	0.00534	0.1616	0.00127	0.6	92.8	785	485	2000-2Dec\ 282.d1.gr6.sp2
2552	22.8	2505	10.4	2468	7.7	99.3	10.79	0.121	0.4857	0.00526	0.1611	0.00073	0.2	103.4	1647	401	2000-2Dec\ 286.d1.gr13.sp1
2439	22.7	2444	10.5	2449	10.7	99.7	10.11	0.115	0.4598	0.00513	0.1594	0.00101	0.1	99.6	989	139	2000-2Dec\ 286.d1.gr14.sp1
2503	31.3	2487	15.5	2473	13.7	99.5	10.58	0.177	0.4744	0.00716	0.1617	0.00131	1.3	101.2	242	338	2000-2Dec\ 286.d1.gr14.sp3
2450	30.7	2470	15.4	2486	11.3	99.5	10.38	0.173	0.4624	0.00697	0.1629	0.00109	0.3	98.6	750	223	2000-2Dec\ 286.d1.gr4.sp1
2257	21.6	2367	9.9	2463	7.1	99.8	9.29	0.100	0.4192	0.00475	0.1607	0.00067	0.6	91.6	737	448	2000-1Dec\ 281.d7.gr20.sp1
2672	27.2	2569	14.9	2489	12.6	99.4	11.55	0.184	0.5136	0.00638	0.1632	0.00122	0.5	107.4	705	356	2000-1Dec\ 281.d7.gr5.sp2
2602	21.0	2532	7.9	2476	7.9	99.8	11.11	0.094	0.4974	0.00488	0.1620	0.00076	0.2	105.1	1176	281	2000-30Nov\ 282.d7.gr1.sp1
2631	16.7	2550	8.5	2487	7.5	99.7	11.32	0.104	0.5040	0.00390	0.1630	0.00073	0.5	105.8	747	391	2000-30Nov\ 282.d7.gr1.sp2
2525	38.4	2496	18.6	2473	18.0	99.3	10.68	0.214	0.4794	0.00881	0.1616	0.00173	1.4	102.1	133	210	2000-30Nov\ 282.d7.gr4.sp1
2536	30.9	2502	15.9	2474	10.7	99.7	10.75	0.184	0.4821	0.00710	0.1618	0.00103	0.5	102.5	519	258	2000-30Nov\ 282.d7.gr4.sp2
2541	46.7	2498	22.9	2464	16.7	99.2	10.71	0.264	0.4832	0.01070	0.1608	0.00159	1.1	103.1	219	265	2000-30Nov\ 282.d7.gr6.sp1
2750	18.4	2603	7.3	2490	4.6	99.9	11.98	0.094	0.5321	0.00438	0.1633	0.00044	0.6	110.4	2257	1500	2000-30Nov\ 282.d7.gr7.sp1
2711	14.5	2602	6.7	2518	6.4	99.6	11.97	0.085	0.5228	0.00342	0.1660	0.00063	0.5	107.7	1801	919	2000-30Nov\ 282.d7.gr9.sp1
2514	55.7	2507	26.7	2502	10.1	99.9	10.81	0.310	0.4769	0.01280	0.1645	0.00099	0.8	100.5	515	444	2000-30Nov\ 283.d7.gr10.sp2
2388	25.3	2437	13.7	2478	11.3	99.6	10.02	0.149	0.4484	0.00568	0.1621	0.00108	0.9	96.4	456	426	2000-30Nov\ 283.d7.gr18.sp1
2424	29.4	2461	16.4	2492	13.5	99.4	10.29	0.182	0.4566	0.00665	0.1635	0.00131	0.7	97.3	431	310	2000-30Nov\ 283.d7.gr3.sp1
2459	20.3	2477	11.4	2491	9.1	99.7	10.46	0.129	0.4643	0.00460	0.1634	0.00089	0.6	98.7	338	227	2000-30Nov\ 283.d7.gr4.sp1
2462	23.8	2464	11.6	2466	8.4	99.8	10.32	0.130	0.4650	0.00541	0.1610	0.00080	0.1	99.8	571	56	2000-30Nov\ 283.d7.gr5.sp1
2529	46.9	2493	26.8	2463	26.1	99.1	10.65	0.307	0.4803	0.01080	0.1607	0.00249	4.0	102.7	74	325	2000-30Nov\ 286.d7.gr5.sp2b
2516	15.9	2503	7.6	2492	4.7	100.0	10.76	0.088	0.4774	0.00365	0.1635	0.00046	0.1	101.0	784	93	2001-10Apr\ 281.d1.gr6.sp1
2520	11.6	2499	5.5	2482	5.9	100.0	10.72	0.063	0.4783	0.00266	0.1625	0.00057	0.5	101.5	754	444	2001-10Apr\ 286.d1.gr5.sp1
2508	13.3	2493	6.3	2482	8.0	99.3	10.65	0.072	0.4755	0.00305	0.1625	0.00077	0.7	101.0	877	687	2001-10Apr\ 281.d1.gr15.sp1r
2522	13.7	2501	7.6	2485	6.1	100.0	10.74	0.087	0.4788	0.00313	0.1628	0.00059	0.6	101.5	939	598	2001-10Apr\ 283.d1.gr6.sp2

[a] Uncertainties listed at the 1σ level.

[b] Correction for common Pb made using the measured $^{204}Pb/^{206}Pb$ ratio.

[c] Th/U calculated using Th^+/U^+ versus Th/U atomic calibration on standard AS3, may differ slightly from Th/U based on calculated semiquantitative Th and U concentrations.

[d] Disc.% is the individual discordance = ($^{206}Pb/^{238}U$ age/$^{207}Pb/^{206}Pb$ age−1 × 100)+100, 100% = concordant analysis after [16].

[e] Semiquantitative estimates based on $U/^{94}Zr_2O$ and $Th/^{94}Zr_2O$ relative to that of measured values of AS3 standard and published U and Th concentrations [33].

Table 6
Zircon U–Pb isotope data from protolith

Ages (Ma)						% Radiogenic $^{206}Pb^{*b}$	Corrected atomic ratios						Th/U[c]	Disc.%[d]	U[e]	Th[e]	Date\ sample#.disc#.grain#.spot#
$^{206}Pb/^{238}U$	±[a]	$^{207}Pb/^{235}U$	±	$^{207}Pb/^{206}Pb$	±		$^{207}Pb^*/^{235}U$	±	$^{206}Pb^*/^{238}U$	±	$^{207}Pb^*/^{206}Pb^*$	±			(ppm)	(ppm)	
2554	8.7	2523	4.2	2497	6.0	100.0	10.99	0.0494	0.4861	0.00201	0.1640	0.00059	0.8	102.3	619	566	2001-10Apr\ 27.d1.gr14.sp1r
2506	23.7	2501	12.4	2497	15.6	99.6	10.75	0.1436	0.4752	0.00543	0.1640	0.00152	3.7	100.4	123	519	2001-10Apr\ 27.d1.gr13.sp1
2467	26.0	2475	12.0	2482	12.2	99.9	10.45	0.1356	0.4662	0.00591	0.1625	0.00118	1.1	99.4	323	404	2001-10Apr\ 27.d1.gr16.sp1
2554	13.6	2522	6.3	2497	6.4	100.0	10.99	0.0748	0.4862	0.00315	0.1640	0.00062	1.2	102.3	412	555	2001-10Apr\ 27.d1.gr16.sp2
2437	16.1	2465	7.7	2487	5.6	100.0	10.33	0.0861	0.4595	0.00365	0.1630	0.00054	0.8	98.0	716	653	2001-10Apr\ 27.d1.gr19.sp1
2479	20.2	2487	9.3	2494	5.8	100.0	10.58	0.1061	0.4689	0.00460	0.1637	0.00056	1.0	99.4	463	557	2001-10Apr\ 27.d1.gr18.sp1
2419	12.8	2457	6.2	2488	6.1	100.0	10.24	0.0681	0.4554	0.00289	0.1631	0.00059	0.7	97.2	693	547	2001-10Apr\ 27.d1.gr10.sp1
2481	8.0	2487	3.6	2491	5.3	100.0	10.58	0.0405	0.4694	0.00183	0.1634	0.00051	0.7	99.6	868	722	2001-10Apr\ 27.d1.gr10.sp2
2379	12.5	2440	6.2	2491	6.1	100.0	10.06	0.0671	0.4464	0.00280	0.1634	0.00059	0.9	95.5	368	388	2001-10Apr\ 27.d1.gr6.sp1
2448	11.8	2468	5.8	2486	7.5	99.9	10.37	0.0652	0.4619	0.00267	0.1629	0.00073	1.0	98.5	483	573	2001-10Apr\ 27.d1.gr6.sp2
2451	10.5	2475	5.4	2495	7.0	99.4	10.45	0.0612	0.4626	0.00238	0.1638	0.00068	0.9	98.2	430	446	2001-10Apr\ 27.d1.gr5.sp1
2500	18.8	2486	9.4	2474	12.1	99.8	10.57	0.1067	0.4737	0.00431	0.1618	0.00116	4.8	101.1	125	695	2001-10Apr\ 27.d1.gr5.sp2
2431	18.1	2471	10.1	2503	13.1	99.7	10.40	0.1132	0.4581	0.00410	0.1646	0.00128	5.8	97.1	70	471	2001-10Apr\ 27.d1.gr9.sp2r
2483	8.0	2491	5.1	2498	8.1	98.5	10.63	0.0582	0.4698	0.00182	0.1640	0.00079	1.1	99.4	398	498	2001-10Apr\ 27.d1.gr9.sp1r
2520	16.9	2496	9.0	2477	13.2	99.8	10.69	0.1031	0.4784	0.00387	0.1620	0.00127	5.8	101.7	95	634	2001-10Apr\ 27.d1.gr12.sp1
2459	12.9	2462	5.7	2465	6.4	100.0	10.30	0.0632	0.4643	0.00294	0.1608	0.00061	0.8	99.8	550	529	2001-10Apr\ 27.d1.gr11.sp1
2495	10.1	2490	5.1	2486	6.5	99.9	10.61	0.0584	0.4727	0.00231	0.1629	0.00063	1.0	100.4	354	411	2001-10Apr\ 27.d1.gr11.sp2
2465	15.1	2477	5.6	2486	10.2	100.0	10.47	0.0630	0.4659	0.00343	0.1629	0.00098	0.9	99.2	767	783	2001-10Apr\ 27.d1.gr8.sp1
2559	15.8	2524	7.4	2495	7.3	99.9	11.00	0.0868	0.4872	0.00366	0.1638	0.00071	0.8	102.6	583	550	2001-10Apr\ 27.d1.gr8.sp2
2510	17.5	2499	8.3	2489	6.1	100.0	10.71	0.0953	0.4761	0.00400	0.1632	0.00059	1.2	100.8	619	858	2001-10Apr\ 27.d1.gr7.sp1
2514	16.9	2492	9.4	2475	14.1	99.8	10.64	0.1075	0.4769	0.00386	0.1618	0.00135	3.6	101.6	125	528	2001-10Apr\ 27.d1.gr17.sp1
2508	11.0	2506	5.5	2505	5.2	99.9	10.80	0.0635	0.4756	0.00252	0.1648	0.00051	0.7	100.1	632	521	2001-10Apr\ 27.d1.gr2.sp3
2477	13.1	2484	7.8	2490	10.0	99.9	10.55	0.0884	0.4685	0.00299	0.1633	0.00097	7.1	99.5	120	974	2001-10Apr\ 27.d1.gr12.sp2
2560	16.2	2521	7.2	2490	6.6	99.7	10.98	0.0844	0.4874	0.00373	0.1633	0.00064	0.8	102.8	593	581	2001-10Apr\ 27.d1.gr11.sp3
2515	15.3	2499	7.3	2487	7.9	100.0	10.72	0.0846	0.4771	0.00352	0.1630	0.00076	1.0	101.1	434	503	2001-10Apr\ 27.d1.gr7.sp2

[a] Uncertainties listed at the 1σ level.

[b] Correction for common Pb made using the measured $^{204}Pb/^{206}Pb$ ratio.

[c] Th/U calculated using Th^+/U^+ versus Th/U atomic calibration on standard AS3, may differ slightly from Th/U based on calculated semiquantitative Th and U concentrations.

[d] Disc.% is the individual discordance = ($^{206}Pb/^{238}U$ age/$^{207}Pb/^{206}Pb$ age−1×100)+100, 100% = concordant analysis after [16].

[e] Semiquantitative estimates based on $U/^{94}Zr_2O$ and $Th/^{94}Zr_2O$ relative to that of measured values of AS3 standard and published U and Th concentrations [33].

Table 7a
Zircon U–Pb isotope data from depth profiling

Ages (Ma)						% Radiogenic $^{206}Pb^{*}$ [b]	Corrected atomic ratios						Th/U	U	Analysis run time	Date\ sample#.grain#.spot#
$\frac{^{206}Pb}{^{238}U}$	± [a]	$\frac{^{207}Pb}{^{235}U}$	±	$\frac{^{207}Pb}{^{206}Pb}$	±		$\frac{^{207}Pb^{*}}{^{235}U}$	±	$\frac{^{206}Pb^{*}}{^{238}U}$	±	$\frac{^{207}Pb^{*}}{^{206}Pb^{*}}$	±		(ppm)[c]	(s)	Cycle #
1923	111	1831	63.5	1727	77.3	99.4	5.067	0.380	0.3476	0.02330	0.1057	0.004454	–	185	98	2001-09Apr\ 286.2.1
1838	107	1781	62.5	1715	79.0	99.5	4.777	0.356	0.3299	0.02202	0.105	0.004514	–	170	159	Cycle 2
1893	116	1832	65.7	1764	77.4	99.6	5.078	0.394	0.3413	0.02420	0.1079	0.004570	–	160	220	Cycle 3
1837	114	1775	68.6	1704	88.7	99.3	4.745	0.388	0.3296	0.02354	0.1044	0.005026	–	153	281	Cycle 4
2016	134	1959	73.1	1899	78.3	99.5	5.883	0.496	0.3671	0.02852	0.1162	0.005063	–	155	343	Cycle 5
1781	110	1749	67.1	1711	89.8	99.4	4.599	0.370	0.3183	0.02242	0.1048	0.005118	–	139	404	Cycle 6
1799	113	1809	69.4	1820	88.8	99.3	4.938	0.406	0.3218	0.02326	0.1113	0.005447	–	136	465	Cycle 7
1656	100	1700	68.3	1755	100.0	99.0	4.336	0.359	0.2929	0.02009	0.1074	0.005885	–	126	526	Cycle 8
1797	116	1861	67.6	1932	79.5	99.7	5.248	0.416	0.3215	0.02370	0.1184	0.005259	–	125	587	Cycle 9
1689	105	1769	64.7	1865	83.4	99.6	4.712	0.364	0.2995	0.02108	0.1141	0.005273	–	112	648	Cycle 10
1780	114	1829	66.3	1885	78.6	99.9	5.060	0.396	0.3181	0.02340	0.1154	0.005036	–	109	709	Cycle 11
1736	110	1775	65.6	1822	82.3	99.8	4.745	0.371	0.3090	0.02240	0.1114	0.005049	–	114	770	Cycle 12
1734	111	1816	68.0	1911	86.3	99.6	4.980	0.401	0.3086	0.02253	0.117	0.005623	–	118	831	Cycle 13
1937	134	1911	73.2	1883	80.1	99.8	5.566	0.473	0.3505	0.02800	0.1152	0.005124	–	118	892	Cycle 14

120 s pre-sputtering of zircon surface prior to commencement of analysis.

[a] Uncertainties listed at the 1σ level.

[b] Correction for common Pb made using the measured $^{204}Pb/^{206}Pb$ ratio.

[c] Semiquantitative estimates based on $U/^{94}Zr_2O$ relative to that of measured values of AS3 standard and published U concentrations [33].

Table 7b
Zircon U–Pb isotope data from depth profiling

Ages (Ma)						% Radiogenic $^{206}Pb^{*b}$	Corrected atomic ratios						Th/U	U	Th	Analysis run time	Date\ sample#.disc#.grain#.spot#
$^{206}Pb/^{238}U$	± [a]	$^{207}Pb/^{235}U$	±	$^{207}Pb/^{206}Pb$	±		$^{207}Pb^*/^{235}U$	±	$^{206}Pb^*/^{238}U$	±	$^{207}Pb^*/^{206}Pb^*$	±		(ppm)[c]	(ppm)[c]	(s)	Cycle #
435	18.1	227.0	149	–	–	81.5	0.251	0.1834	0.06977	0.00300	0.02604	0.018540	0.1	1134	169	98	2001-09Apr\ 286_6_2_3
616	18.8	671.2	81	861.3	314.0	91.1	0.937	0.1540	0.10030	0.00321	0.06776	0.010250	0.1	826	78	159	Cycle 2
829	24.7	895.2	62	1062	190.0	94.8	1.415	0.1484	0.13730	0.00436	0.07474	0.007041	0.1	761	54	220	Cycle 3
923	31.0	1070.0	45	1384	106.0	97.2	1.869	0.1264	0.15390	0.00556	0.08805	0.004878	0.1	673	40	281	Cycle 4
1118	29.5	1243.0	39	1467	86.0	97.9	2.402	0.1295	0.18940	0.00543	0.09197	0.004167	0.1	648	38	342	Cycle 5
1182	33.5	1341.0	31	1605	58.9	99.1	2.745	0.1153	0.20120	0.00624	0.09897	0.003124	0.1	610	37	403	Cycle 6
1167	34.6	1355.0	30	1667	52.7	99.4	2.799	0.1132	0.19840	0.00644	0.10230	0.002913	0.1	668	45	465	Cycle 7
1134	39.6	1328.0	33	1655	50.5	99.5	2.698	0.1187	0.19240	0.00732	0.10170	0.002772	0.1	677	61	526	Cycle 8
1100	45.5	1324.0	37	1708	50.2	99.6	2.684	0.134	0.18600	0.00837	0.10460	0.002852	0.1	611	83	587	Cycle 9
1151	39.0	1347.0	33	1674	53.8	99.4	2.768	0.1226	0.19550	0.00722	0.10270	0.002988	0.2	610	109	648	Cycle 10
1154	47.0	1327.0	38	1617	58.1	99.3	2.694	0.1395	0.19610	0.00871	0.09963	0.003107	0.2	535	122	709	Cycle 11
1203	49.4	1368.0	39	1635	59.2	99.3	2.847	0.1494	0.20520	0.00924	0.10060	0.003205	0.3	483	152	770	Cycle 12
1265	48.1	1403.0	39	1619	62.8	99.2	2.980	0.1521	0.21670	0.00908	0.09972	0.003365	0.4	463	162	831	Cycle 13
1245	57.8	1447.0	43	1757	55.8	99.5	3.156	0.1777	0.21300	0.01088	0.10750	0.003280	0.4	424	185	892	Cycle 14
1280	60.6	1433.0	44	1667	58.8	99.5	3.100	0.1789	0.21970	0.01146	0.10230	0.003254	0.5	414	205	953	Cycle 15
1584	67.3	1669.0	44	1777	57.8	99.5	4.174	0.2256	0.27860	0.01335	0.10870	0.003445	0.6	426	248	1079	Cycle 16
1533	56.4	1642.0	39	1786	56.8	99.7	4.041	0.1914	0.26840	0.01110	0.10920	0.003405	0.7	380	249	1140	Cycle 17
1521	58.5	1638.0	39	1793	54.5	99.8	4.021	0.1927	0.26600	0.01150	0.10960	0.003281	0.7	361	247	1201	Cycle 18
1566	65.6	1651.0	43	1761	59.3	99.7	4.083	0.2164	0.27490	0.01297	0.10770	0.003496	0.7	356	261	1262	Cycle 19
1496	53.9	1630.0	38	1806	58.7	99.8	3.978	0.1836	0.26130	0.01055	0.11040	0.003567	0.8	331	265	1323	Cycle 20
1532	66.0	1652.0	44	1808	61.3	99.7	4.089	0.2223	0.26830	0.01298	0.11050	0.003728	0.8	328	267	1385	Cycle 21
1630	83.1	1707.0	54	1803	68.2	99.4	4.371	0.2847	0.28770	0.01660	0.11020	0.004135	0.9	300	271	1446	Cycle 22
1506	58.4	1636.0	41	1808	64.1	99.8	4.010	0.2006	0.26310	0.01144	0.11050	0.003900	1.0	275	278	1507	Cycle 23
1475	58.0	1599.0	41	1767	65.8	99.8	3.830	0.1936	0.25710	0.01130	0.10800	0.003890	1.1	267	299	1568	Cycle 24
1535	63.5	1696.0	43	1901	66.0	99.8	4.314	0.2274	0.26890	0.01250	0.11640	0.004272	1.2	248	300	1629	Cycle 25
1479	63.4	1663.0	45	1903	69.5	99.8	4.143	0.2263	0.25790	0.01236	0.11650	0.004507	1.3	233	306	1751	Cycle 27
1643	77.7	1743.0	53	1865	79.3	99.4	4.564	0.2899	0.29020	0.01554	0.11400	0.005011	1.4	217	297	1812	Cycle 28
1502	68.2	1642.0	47	1826	73.9	99.8	4.040	0.2331	0.26250	0.01335	0.11160	0.004553	1.5	220	327	1874	Cycle 29
1519	74.0	1693.0	50	1915	74.4	99.8	4.298	0.2606	0.26580	0.01452	0.11730	0.004865	1.6	204	325	1935	Cycle 30
1570	79.9	1684.0	65	1827	110.0	98.6	4.249	0.3355	0.27590	0.01581	0.11170	0.006770	1.7	175	296	2183	Cycle 33
1573	79.3	1701.0	58	1862	93.4	99.3	4.339	0.3058	0.27640	0.01570	0.11390	0.005893	1.9	164	306	2244	Cycle 34
1523	79.5	1692.0	60	1908	95.7	99.2	4.292	0.3111	0.26660	0.01562	0.11680	0.006223	2.0	148	298	2366	Cycle 36

No pre-sputtering of zircon surface prior to commencement of analysis.

[a] Uncertainties listed at the 1σ level.

[b] Correction for common Pb made using the measured $^{204}Pb/^{206}Pb$ ratio.

[c] Semiquantitative estimates based on $U/^{94}Zr_2O$ and $Th/^{94}Zr_2O$ relative to that of measured values of AS3 standard and published U and Th concentrations [33].

fluid infiltration also lends support to the above model. We conclude that the isotopic response of zircon appears to be strongly controlled by the interaction of an aqueous fluid, of low to moderate salinity, along penetrative micro-fracture networks, during prevailing upper-amphibolite facies conditions.

5.4. Grain-scale Pb redistribution

Overall, however, on the grain scale, one would expect that zircon would tend to either remain a closed system or, more likely, lose some accumulated Pb* during geological disturbance (though this may not be necessarily always so [6]). Whole grain dissolution analyses of zircon, therefore, would be concordant, or, to some degree, normally discordant. We might, therefore, expect that a pooled average of the U/Pb data ($n = 31$ from the alteration selvedge; $n = 25$ from the protolith; Tables 1 and 2) may be considered a reasonable approximation to grain-scale analysis, and should lie on concordia or be normally discordant. Bootstrap replications of the U/Pb data provide an average of the available data. These calculations, shown in Figs. 5 and 6 as shaded ellipses, indicate that average zircon data, from both the alteration selvedge and the protolith, are concordant at the 2σ level. These results confirm that the overall net Pb loss from both zircon populations (alteration selvedge and protolith) has been minor; if Pb loss had been significant *on the grain scale*, we might expect the bootstrap average of these data to fall below concordia.

6. Conclusions

This study examines zircon isotopic response to fluids at elevated metamorphic conditions in a well-defined field setting using both sectioned zircon and depth profiling ion probe techniques. Using conventional ion probe techniques on sectioned zircons, we conclude that zircons hosted within Archaean protolith that interacted with an Early Palaeozoic aqueous fluid, during upper-amphibolite facies conditions, experienced *limited* net loss and gain of Pb* at the subgrain scale, resulting in discordance of 92–110%. At the grain scale, Pb* loss was negligible. In contrast, depth profiling ion probe techniques on natural crystal faces reveal extensive disturbance of near-surface zircon (0–0.25 μm) during the Early Palaeozoic. Important aspects of this study are that the *P–T* conditions and fluid composition to which the zircons were exposed is well constrained, potential effects due to pervasive deformation on zircon systematics are insignificant, and that the relationship between fluid influx at upper-amphibolite facies conditions and near-surface zircon isotopic response is unequivocal.

Although growth of new zircon during fluid infiltration is reported for certain conditions [47], many studies appeal to metamorphic fluids as a means by which zircon isotopic systematics might be easily disturbed, resulting in Pb* loss with complete or significant isotopic resetting. Although such conclusions are supported by the majority of experimental studies on variably radiation-damaged zircon, our field-based study indicates that significant grain-scale isotopic resetting was not achieved during infiltration of a low-salinity aqueous fluid, under *static* upper-amphibolite facies conditions. Infiltrating fluids probably have to operate in concert with other factors, such as pervasive deformation [19], in order to induce wholesale grain-scale isotopic modification in zircon. Isotopic modification is instead controlled by penetrative micro-fracture networks permitting enhanced fluid access, resulting in resetting/recrystallisation/growth along penetrative fracture surfaces and crystal faces. Our findings support the conclusions and suggestions of several previous studies (e.g. [11,20,40]), however, this study utilises direct isotopic measurement of zircon crystal surfaces in support of our conclusions. We advocate caution should be exercised when considering geochronological interpretations that rely on extensive zircon resetting during aqueous fluid–rock interaction at elevated metamorphic grade.

Acknowledgements

C.J.C. acknowledges participation in the 40th Japanese Antarctic Research Expeditions (JARE-

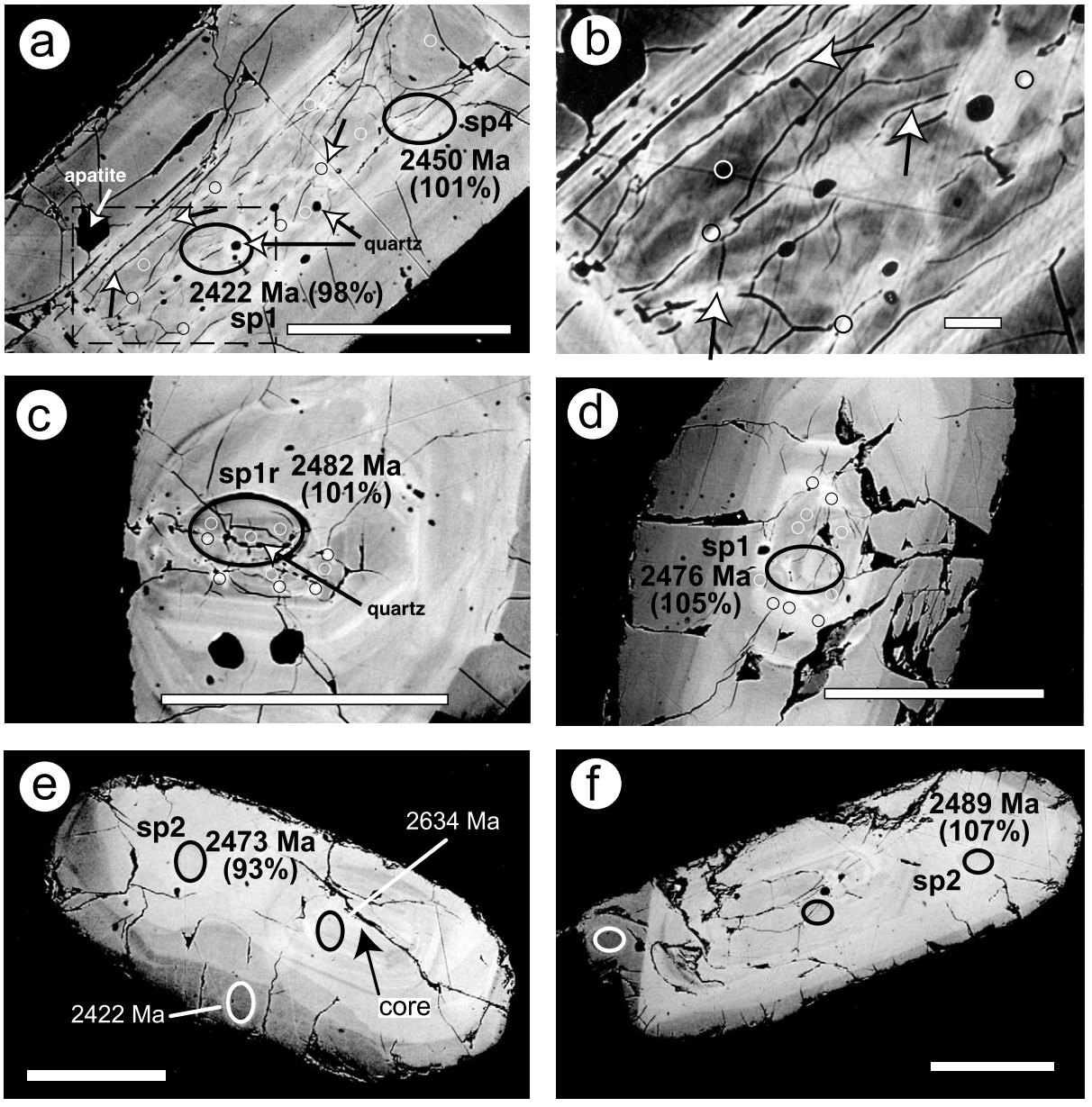

Fig. 8. BSE images of selected zircon core regions (a–d) and whole grains (e,f). Scale bar = 100 μm, except where indicated; analysis sites (ion probe = large ellipses; electron probe = small open circles) and $^{206}Pb/^{207}Pb$ ages are indicated. (a) Zircon analyses 28/1.d1.gr3, sp1 and sp4 have U contents (ion probe measurements) of 902 and 1047 ppm respectively. (b) Enlargement of dashed area indicated in panel a, note in particular the association of fractures with enrichment of U, Pb and Th (unlabelled arrows), linear features are surface scratches from polishing. (c) Zircon analysis 28/1.d1.gr15, sp1r = 1176 ppm U. (d) Zircon analysis 28/2.d7.gr1, sp1 = 877 ppm U. (e) Zircon analysis 28/2.d1.gr14, sp2 = 785 ppm U. (f) Zircon analysis 28/1.d7.gr5, sp2 = 705 ppm. Although analyses shown in panels a and c are mildly discordant (98–101%), in core regions irregular compositional heterogeneity are clearly visible in panels a–d as mottled light (elevated U and Pb) and dark regions (U and Pb poor regions); a relationship with internal fractures and observed compositional variability is clearly discernible. In contrast, analyses indicated in panels e and f, which are significantly discordant (93% and 107% respectively), show no readily apparent compositional or internal structural features that might contribute to the observed discordance.

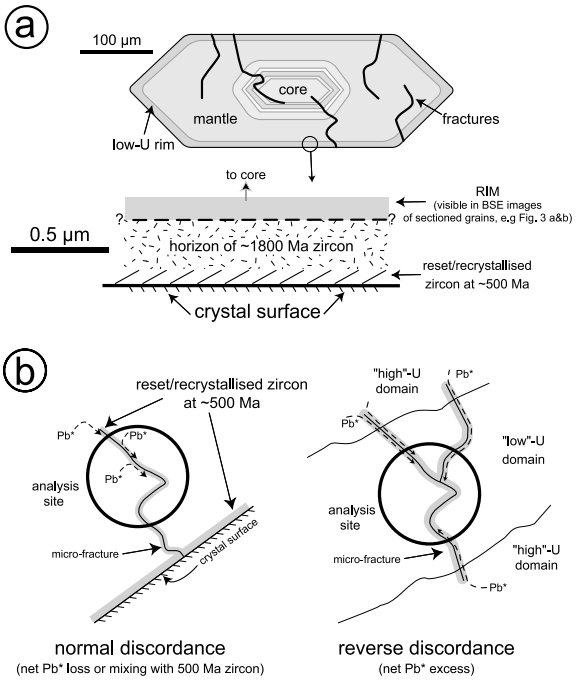

Fig. 9. (a) Schematic diagram summarising the features of zircon morphology (illustrating core, mantle and outer rim as discussed in the text) and near-surface chronological architecture as determined from depth profiling ion probe analysis. The majority of analyses from sectioned grains preserve $^{206}Pb/^{207}Pb$ ages between 2446 and 2518 Ma (Tables 5 and 6), although several core analyses record $^{206}Pb/^{207}Pb$ ages ~2626 Ma (Carson, unpublished data). The surface region is characterised by a near-surface film of reset/recrystallised or new zircon at the sub-micrometre scale, ~500 Ma in age, underlain by a horizon of ~1800 Ma of undetermined thickness. (b) Highly schematic micro-fracture-based model for yielding discordant ion probe analysis; normal discordance may result from analytical mixing of zircon of ~500 Ma age immediately adjacent to micro-fractures with that of surrounding unaltered zircon of ~2480 Ma. Reverse discordance may result from migration of Pb* from high-U domains (=high Pb*) into low-U domains (=low Pb*) along micro-fractures, which may locally fortuitously result in unsupported Pb* accumulations, on the scale of an ion probe analysis.

40) and the SEAL (Structure and Evolution of east Antarctic Lithosphere) programme, at the kind invitation of K. Shiraishi and Y. Motoyoshi of the National Institute of Polar Research, Tokyo. C.J.C. also expresses thanks to the expeditioners of JARE-39 and 40, particularly the Tonagh Island field party, and the officers and crew of the Icebreaker *Shirase*, for the hospitality extended to him during JARE-40. Assistance by and discussion with K. McKeegan and C.M. Breeding during ion probe sessions at the Department of Earth and Space Sciences, UCLA, and with J. Eckert during electron microprobe sessions at Yale University is appreciated. R.A. Stern provided valuable insight into the minutiae of ion probe calibrations. E.S. Grew provided the photograph in Figure 2. Ian Williams and Klaus Mezger are thanked for detailed comments on an earlier version of the manuscript. Simon Harley, Urs Schaltegger and Randy Parrish are thanked for providing thoughtful, constructive and insightful reviews which greatly improved the final manuscript. C.J.C. acknowledges receipt of the Damon Wells '58 postdoctoral fellowship whilst at Yale University; analytical costs supported by National Science Foundation Grants EAR-0001084 and EAR-9810089.*[AH]*

Appendix. Petrology and whole rock geochemistry

Petrology

Pyroxene-bearing quartzo-feldspathic orthogneiss, the protolith in this study, is a common lithology on Tonagh Island. The unit is light brown- to buff-coloured, massive in outcrop with a well-developed gneissosity defined by 1–10 mm scale discontinuous quartzo-feldspathic segregations. At the sampling location, the visible alteration extends 1 m either side of the pegmatite (sample 29), illustrated in Fig. 2. The protolith is equigranular (~0.5–1 mm) and comprised of quartz (~33% mode), alkali-feldspar (~16%; $Or_{90}Ab_9$) and plagioclase (~22–25%; ~An_{30}) and subhedral mesoperthite (~22% with 48:52 ratio of plagioclase to alkali feldspar). Orthopyroxene (3–5%; X_{Fe} ~0.49) and clinopyroxene (≤1%) occur as dispersed subhedral grains, with rare development of discontinuous fringes of hornblende. Magnetite–ilmenite pairs (~1% mode) are rarely mantled by unorientated biotite. Accessory apatite (≤1%) occurs as dispersed subhedral grains. Monazite growth on apatite may be present.

The visible transition in the field from buff-col-

oured to light grey orthogneiss marks the pyroxene-out isograd (Fig. 2). Just within the visible alteration selvedge, pyroxene is pseudomorphed by aggregates of hornblende–quartz. Biotite coronas on magnetite–ilmenite pairs are well-developed, as are isolated aggregates of unorientated biotite. Hornblende reaches maximum mode at ~4% then decreases in abundance toward the pegmatite. Biotite modal abundance increases progressively. Plagioclase and alkali-feldspar exhibit considerable recrystallisation and sub-grain development. Alkali-feldspar decreases significantly in modal abundance to ~7%; mesoperthite to ~10% and the proportion of alkali-feldspar in mesoperthite decreases to 40%. Mesoperthite alkali-feldspar lamellae begin to show evidence of resorption and adopt a ragged appearance. Plagioclase remains approximately constant mode (~25%) but exhibits progressive compositional change from the protolith (An_{30}) to An_{22} adjacent to the pegmatite. Euhedral epidote may be associated with biotite aggregates. Epidote growth on apatite becomes increasingly common. Monazite, either as isolated grains or as growths on apatite, is not observed *within* the alteration selvedge. Immediately adjacent to the pegmatite (sample 28/6), hornblende and ilmenite are absent, biotite reaches ~20% mode. Magnetite occurs as either skeletal or rounded grains with quartz inclusions, but, in both cases, associated with biotite. No deformation fabric or preferred orientation of matrix grains is present suggesting that metasomatism and pegmatite emplacement is not accompanied by significant deformation.

Whole rock geochemistry

A detailed description of the whole rock geochemistry of both alteration selvedge and protolith will be presented elsewhere and only a brief summary is offered here. The mass change estimates listed below are based on both Ti and Al (as assumed *relatively* immobile geochemical reference frames; e.g. [48]) and elemental concentration ratios (the ratio of species in the altered unit relative that of the reference protolith; e.g. [49]). Both techniques provide compatible results. The alteration selvedge shows mass *addition* of Na_2O (15–20%), Rb (~80%), P_2O_5 (~20%), Th (~120%), U (~100%) and Pb (~90%). Rare earth elements (ΣREEs ~30–40%) and Y (~75%) also show significant enrichment, with preferential enrichment of the HREEs with increasing alteration. The alteration selvedge underwent mass *loss* of CaO (~15%), Sr (~20%), Ba (~20%) and K_2O (~25%). Negligible mass change (< 5%) is exhibited by SiO_2, TiO_2, Al_2O_3, MgO and Zr. Total mass change experienced by the alteration selvedge is negligible. Density contrast between the protolith and alteration selvedge is insignificant, ranging between ~2.69 and 2.67 g/cc.

References

[1] D. Gebauer, M. Grünenfelder, U-Pb zircon and Rb-Sr whole-rock dating of low-grade metasediments example: Montagne Noire (southern France), Contrib. Mineral. Petrol. 59 (1976) 13–32.
[2] K. Mezger, E.J. Krogstad, Interpretation of discordant U-Pb zircon ages: An evaluation, J. Metamorph. Geol. 15 (1997) 127–140.
[3] G.W. Wetherill, Discordant uranium-lead ages, Trans. Am. Geophys. Union 37 (1956) 320–326.
[4] G.R. Tilton, Volume diffusion as a mechanism for discordant lead ages, J. Geophys. Res. 65 (1960) 2933–2945.
[5] I.S. Williams, W. Compston, L.P. Black, T.R. Ireland, J.J. Foster, Unsupported radiogenic Pb in zircon: a cause of anomalously high Pb-Pb, U-Pb and Th-Pb ages, Contrib. Mineral. Petrol. 88 (1984) 322–327.
[6] J.M. Mattinson, C.M. Graubard, D.L. Parkinson, W.C. McClelland, U-Pb reverse discordance in zircons: the role of fine scale oscillatory zoning and submicron transport of Pb, Geophys. Monogr. 95 (1996) 355–370.
[7] D.J. Cherniak, E.B. Watson, Pb diffusion in zircon, Chem. Geol. 172 (2000) 5–24.
[8] J.K.W. Lee, I.S. Williams, D.J. Ellis, Pb, U and Th diffusion in natural zircon, Nature 390 (1997) 159–161.
[9] A.K. Sinha, D.M. Wayne, D.A. Hewitt, The hydrothermal stability of zircon: preliminary experimental and isotopic studies, Geochim. Cosmochim. Acta 56 (1992) 3551–3560.
[10] J.K.W. Lee, Multipath diffusion in geochronology, Contrib. Mineral. Petrol. 120 (1995) 60–82.
[11] T.E. Krogh, G.L. Davis, Alteration in zircons with discordant U-Pb ages, Carnegie Inst. Washington Yearb. 73 (1974) 560–567.
[12] K. Högdahl, L.P. Gromet, C. Broman, Low P-T Caledonian resetting of U-rich Paleoproterozoic zircons, central Sweden, Am. Mineral. 86 (2001) 534–546.

[13] R.T. Pidgeon, J.R. O'Neil, L.T. Silver, Uranium and lead isotopic stability in a metamict zircon under experimental hydrothermal conditions, Science 154 (1966) 1538–1540.
[14] N.G. Rizvanova, O.A. Levchenkov, A.E. Belous, N.I. Bezmen, A.V. Maslenikov, A.N. Komarov, A.F. Makeev, L.K. Levskiy, Zircon reaction and stability of the U-Pb isotope system during interaction with carbonate fluid: experimental hydrothermal study, Contrib. Mineral. Petrol. 139 (2000) 101–114.
[15] T. Geisler, M. Ulonska, H. Schleicher, R.T. Pidgeon, W. van Bronswijk, Leaching and differential recrystallization of metamict zircon under experimental hydrothermal conditions, Contrib. Mineral. Petrol. 141 (2001) 53–65.
[16] C.R.L. Friend, A.P. Nutman, Response of zircon U-Pb isotopes and whole-rock geochemistry to CO_2 fluid-induced granulite-facies metamorphism, Kabbaldurga, Karnataka, South India, Contrib. Mineral. Petrol. 111 (1992) 299–310.
[17] J. Konzett, R.A. Armstrong, R. Sweeney, W. Compston, The timing of MARID metasomatism in the Kaapvaal mantle: an ion probe study of zircons from MARID xenoliths, Earth Planet. Sci. Lett. 160 (1998) 133–145.
[18] U. Schaltegger, C.M. Fanning, D. Günther, J.C. Maurin, K. Schulmann, D. Gebauer, Growth, annealing and recrystallization of zircon and preservation of monazite in high-grade metamorphism: conventional and in-situ U-Pb isotope, cathodoluminesence and microchemical evidence, Contrib. Mineral. Petrol. 134 (1999) 186–201.
[19] G. Vavra, R. Schmid, D. Gebauer, Internal morphology, habit and U-Th-Pb microanalysis of amphibolite-to-granulite facies zircons: geochronology of the Ivera Zone (Southern Alps), Contrib. Mineral. Petrol. 134 (1999) 380–404.
[20] S.L. Harley, I. Snape, L.P. Black, The evolution of a layered metaigneous complex in the Rauer Group, East Antarctica: evidence for a distinct Archaean terrane, Precambrian Res. 89 (1998) 175–205.
[21] D.M. Wayne, A.K. Sinha, Physical and chemical response of zircons to deformation, Contrib. Mineral. Petrol. 98 (1988) 109–121.
[22] S.L. Harley, B.J. Hensen, Archaean and Proterozoic high-grade terranes of East Antarctica (40°E–60°E): A case study of the diversity in granulite facies metamorphism, in: J.R. Ashworth, M. Brown (Eds.), High Temperature Metamorphism and Crustal Anatexis, Unwin Hyman, London, 1990, pp. 320–370.
[23] E.S. Grew, W.I. Manton, Archaean rocks in Antarctica 2.5-billion-year uranium-lead ages of pegmatites in Enderby Land, Science 206 (1979) 443–445.
[24] L.P. Black, P.R. James, S.L. Harley, Geochronology and geological evolution of metamorphic rocks in the Field Islands area, East Antarctica, J. Metamorph. Geol. 1 (1983) 277–303.
[25] J.W. Sheraton, R.J. Tingey, L.P. Black, L.A. Offe, D.J. Ellis, Geology of Enderby Land and western Kemp Land, Antarctica, Bur. Mineral Resources, Australia, Bull. 223 (1987) 51 pp.
[26] Y. Osanai, T. Toyoshima, M. Owada, T. Tsunogae, T. Hokada, W.A. Crowe, Geology of ultrahigh-temperature metamorphic rocks from Tonagh Island in the Napier Complex, East Antarctica, Polar Geosci. 12 (1999) 1–28.
[27] R. Powell, T.J.B. Holland, Optimal geothermometry and geobarometry, Am. Mineral. 79 (1994) 120–133.
[28] C. Zhu, D.A. Sverjensky, F-Cl-OH partitioning between biotite and apatite, Geochim. Cosmochim. Acta 56 (1992) 3435–3467.
[29] T.D. Peterson, A refined technique for measuring crystal size distributions in thin section, Contrib. Mineral. Petrol. 124 (1996) 395–405.
[30] M. Grove, T.M. Harrison, Monazite Th-Pb age depth profiling, Geology 27 (1999) 487–490.
[31] X. Quidelleur, M. Grove, O.M. Lovera, T.M. Harrison, A. Yin, F.J. Ryerson, The thermal evolution and slip history of the Renbu Zedong Thrust, southeastern Tibet, J. Geophys. Res. 102 (1997) 2659–2679.
[32] K.R. Ludwig, User's Manual for Isoplot/Ex, v2.3, A Geochronological Toolkit for Microsoft Excel, Geochronological Centre Special Publication, 1a, Berkeley, CA, 1999, 54 pp.
[33] J.B. Paces, J.D. Miller, Precise U-Pb ages of Duluth Complex and related mafic intrusions, Northeastern Minnesota: geochronological insights to physical, petrogenetic, paleomagnetic, and tectonomagnetic processes associated with the 1.1 Ga midcontinental rift system, J. Geophys. Res. 98 (1993) 13997–14013.
[34] G.M. Dipple, J.M. Ferry, Metasomatism and fluid flow in ductile fault zones, Contrib. Mineral. Petrol. 112 (1992) 149–164.
[35] L.P. Black, I.S. Williams, W. Compston, Four zircon ages from one rock: the history of a 3930 Ma old granulite from Mt Sones, Enderby Land, Antarctica, Contrib. Mineral. Petrol. 94 (1986) 427–437.
[36] K.R. Ludwig, On the treatment of concordant uranium-lead ages, Geochim. Cosmochim. Acta 62 (1998) 315–318.
[37] B. Efron, R.J. Tibshirani, An Introduction to the Bootstrap, Chapman and Hall, New York, 1993, 436 pp.
[38] E.S. Grew, K. Suzuki, M. Asami, CHIME ages of xenotime, monazite and zircon from beryllium pegmatites in the Napier Complex, East Antarctica, Polar Geosci. 14 (2001) 99–118.
[39] M. Owada, Y. Osanai, T. Tsunogae, T. Hamamoto, H. Kagami, T. Toyoshima, T. Hokada, Sm-Nd garnet ages of retrograde garnet bearing granulites from Tonagh Island in the Napier Complex, East Antarctica: a preliminary study, Polar Geosci. 14 (2001) 75–87.
[40] T.E. Krogh, Improved accuracy of U-Pb ages by the creation of more concordant systems using an air abrasion technique, Geochim. Cosmochim. Acta 46 (1982) 637–649.
[41] L.P. Black, P.D. Kinny, J.W. Sheraton, The difficulties of dating mafic dykes: an Antarctic example, Contrib. Mineral. Petrol. 109 (1991) 183–194.
[42] A.C. McLaren, J.D. Fitzgerald, I.S. Williams, The microstructure of zircon and its influence on the age determi-

nation from Pb/U isotopic ratios measured by ion microprobe, Geochim. Cosmochim. Acta 58 (1994) 993–1005.
[43] M. Wiedenbeck, An example of reverse discordance during ion microprobe zircon dating – an artifact of enhanced ion yields from a radiogenic labile Pb, Chem. Geol. 125 (1995) 197–219.
[44] J.K.W. Lee, Problems and progress in the elucidation of U and Pb transport mechanisms in zircon, in: J.N. Boland, J.D. Fitz Gerald (Eds.), Defects and Processes in the Solid State: Geoscience Applications, The McLaren Volume, Elsevier, Amsterdam, 1993, pp. 423–446.
[45] J.K.W. Lee, J. Tromp, Self-induced facture generation in zircon, J. Geophys. Res. 100 (1995) 17753–17770.
[46] A. Meldrum, L.A. Boatner, W.J. Weber, R.C. Ewing, Radiation damage in zircon and monazite, Am. Mineral. 62 (1998) 2509–2520.
[47] P.K. Zeitler, B. Barreiro, C.P. Chamberlain, D. RumbleIII, Ion-microprobe dating of zircon from quartz-graphite veins at the Bristol, New Hampshire, metamorphic hot spot, Geology 18 (1990) 626–629.
[48] J.J. Ague, Mass transfer during Barrovian metamorphism of pelites, south-central Connecticut. I: Evidence for changes in composition and volume, Am. J. Sci. 294 (1994) 989–1057.
[49] J.J. Ague, J.L.M. van Haren, Assessing metasomatic mass and volume changes using the Bootstrap, with application to deep crustal hydrothermal alteration of marble, Econ. Geol. 91 (1996) 1169–1182.